HYDROGEOLOGIC MODEL OF GROUNDWATER FLOW WITHIN MOUNT ST. HELENS VOLCANO DETERMINED FROM SELF-POTENTIAL AND TIME-DOMAIN ELECTROMAGNETIC MEASUREMENTS

by

Alicia Hotovec

A thesis submitted to the Faculty and the Board of Trustees of the Colorado School of Mines in partial fulfillment of the requirements for the degree of Master of Science (Geophysics).

Golden, Colorado
Date: _____

Signed: _____
Alicia Hotovec

Signed: _____
Dr. André Revil
Thesis Advisor

Golden, Colorado
Date: _____

Signed: _____
Dr. T. K. Young
Professor and Head
Department of Geophysics

ABSTRACT

Knowledge of groundwater flow due to hydrothermal circulation in volcanoes is important in evaluating the risk of volcanic activity and potential flank collapses. Indeed, hydrothermal alteration can weaken slopes and increase risk of collapse during eruptions. Unfortunately, hydrothermal systems are complex and difficult to image in volcanic areas. Self-potential is a passive electrical method that is sensitive to groundwater flow. This method can therefore be used to understand the pattern of the hydrothermal systems. The self-potential method requires only light equipment that is easy to use in the difficult field conditions of active volcanoes.

Self-potential measurements were taken on Mount St. Helens volcano in 2000, 2001, and 2007. Mount St. Helens is of particular interest because the north flank of the volcano was removed in a large-scale sector collapse in 1980, allowing a deeper look into the structure of the volcano. These measurements were accompanied by time-domain electromagnetic (TDEM) measurements, which provide information about the resistivity structure. The self-potential signal combined with local geology and resistivity structure allows a rudimentary hydrogeologic model of Mount St. Helens to be built. This model was then tested using COMSOL Multiphysics®, a commercial finite-element modeling program, to reproduce the self-potential data. Modeling indicates that the large negative anomaly (800 mV) near the dome is likely caused by downward flow through the Rampart Fault, a large fracture that was visible at the surface following the 1980 eruption.

TABLE OF CONTENTS

LIST OF FIGURES

LIST OF TABLES

ACKNOWLEDGEMENTS

First and foremost, I would like to thank my advisor, Dr. André Revil, and my committee, Dr. Adel Zohdy and Dr. Dave Hale, for their insight and wisdom. I have learned so much from each of you.

This entire project would not have been possible without the help of Dr. Paul Bedrosian. Thank you for deciding to take me along, giving me the opportunity to work in such an amazing field area, and organizing the project. On a related note, I would like to thank Matt Burgess and Dr. Jeff Wynn for their help out in the field acquiring data.

Special thanks are extended to Cynthia Gardner, who let us work on Mount St. Helens in the first place, and to my mentor, Dr. John Pallister, who graciously let me live with him while in Washington and offered extremely useful knowledge of the field.

Financial support for my research was provided by the Department of Geophysics in the form of teaching assistantships. Further support for travel expenses were provided by the USGS Mentoring Program.

Finally, I offer my deepest and sincere gratitude to my friends and family. I would have accomplished nothing without your unending support and encouragement.

CHAPTER 1

INTRODUCTION

Determining the location of aquifers and the structure of groundwater flow due to hydrothermal circulation in volcanoes is important in evaluating volcanic hazards. Indeed, aquifers may interact with magmatic intrusions and produce explosive phreatomagmatic eruptions (White, 1996). Perhaps more threatening is large-scale flank collapse due to hydrothermal alteration.

Flank collapse is a prominent occurrence on stratovolcanoes, often accompanying eruptive activity (López and Williams, 1993). On Mount St. Helens, flank collapse resulting in rapid unloading of the hydrothermal and magmatic system caused the main lateral blast on May 18, 1980 (Lipman and Mullineaux, 1981; Siebert et al., 1987). Similar flank collapses have been documented on several other stratovolcanoes such as Mount St. Augustine (Alaska), Bezymianny (Russia), and Unzen (Japan). Although flank collapses may occur concurrently with active eruptions, there have been many cases, such as on Bandai-san (Japan) in 1888, where the flank collapse did not accompany the injection of new magma into the system (Siebert et al., 1987).

Hydrothermal alteration leads to these kinds of collapses when dissolution of the volcanic glass and precipitation of clays and zeolites occurs on gravitationally unstable fault planes, and is especially dangerous when combined with steep slopes (Reid et al., 2001). Hydrothermal alteration is caused by the chemical weathering of rock minerals by heated water in the hydrothermal system, and produces rocks with reduced mechanical strength. In order to better understand the extent of ongoing hydrothermal alteration

beyond surface observations, we must understand the layout of the subsurface hydrothermal system itself. However, hydrothermal systems in volcanoes are complex, partially due to their irregularly stratified nature from thousands of years of overlapping lava and pyroclastic flows. Unfortunately, the finer scale structures of most volcanoes are not well understood because studies are difficult to undertake given the large scale required over rugged, often dangerous topography.

One of the few geophysical methods well-suited to volcanic applications in the field is the self-potential method. The equipment required for self-potential measurements is lightweight and portable over volcanic terrain, and consists of a pair of non-polarizing electrodes and a high-impedance voltmeter. The method itself can partially answer the question of where the groundwater is flowing in a volcanic hydrothermal system because of its correlation to groundwater flow. Through electrokinetic coupling between the Darcy velocity and the electrical current density, self-potential is sensitive to the pattern of groundwater flow (Rizzo et al., 2004). Other effects, such as electrochemical and thermoelectric effects also contribute to the overall self-potential signal, but their contributions, which are on the order of a few tens of mV to a few hundred mV, are small compared to the several hundreds of mV produced by electrokinetic effects on volcanoes in particular (Corwin and Hoover, 1979; Zlotnicki and Nishida, 2003).

The source of electrokinetic coupling stems from the flow of water in the pore space. The pore wall is slightly electrically charged, and attracts ions from the pore water. These ions create a thin, electrically charged layer near the pore wall, and the flow of water drags the excess of these ionic charges and generates an electrical source current. In turn, this source of current creates an electrical field in the conductive space. In a volcanic

hydrothermal system, water is introduced into the system by rainfall, other deep aquifers, or by the cooling of magma and is recycled within the hydrothermal cell. Water is heated by magma from below and rises toward the surface, creating a positive self-potential anomaly. Then, as the water cools, it runs down the flanks of the volcano through cracks and permeable layers, and creates a negative self-potential anomaly. Often along the flanks of volcanoes there is a purely hydrogeological inverse correlation between topography and self-potential known as the topographic effect, where water flows along subhorizontal layers with similar topography to the surface (Zlotnicki and Nishida, 2003). Figure 1.1 is a rudimentary illustration of the basic shape of the self-potential anomaly most commonly seen on volcanic edifices driven by upward flow through a conduit and downward flow driven by topography. Of course, the shape of the self-potential anomaly is not only sensitive to groundwater flow, which varies widely from volcano to volcano, but also underlying electrical conductivity structure because it affects the equipotential distribution on the surface and throughout the structure (Ishido, 2004).

The self-potential method has been used to study many volcanoes with a wide range of results. Large self-potential anomalies have been documented on many volcanoes in Japan including Mt. Fuji (Aizawa, 2004; Aizawa et al., 2005), Iwate, Iwaki, Nantai, Nikko-Shirane (Aizawa et al., 2009), Aso (Hase et al., 2005), and Miyake-jima (Zlotnicki et al., 2003), as well as on volcanoes around the world such as Misti in Peru (Finizola et al., 2004), Piton de la Fournaise in Réunion (Michel and Zlotnicki, 1998), and Vesuvius (Di Maio et al. 1998), Vulcano (Barde-Cabusson et al., 2009), and Stromboli (Finizola et al., 2002; Finizola et al., 2003) in Italy. The cause for these self-potential anomalies varies from case to case. For example, several positive anomalies were mapped on

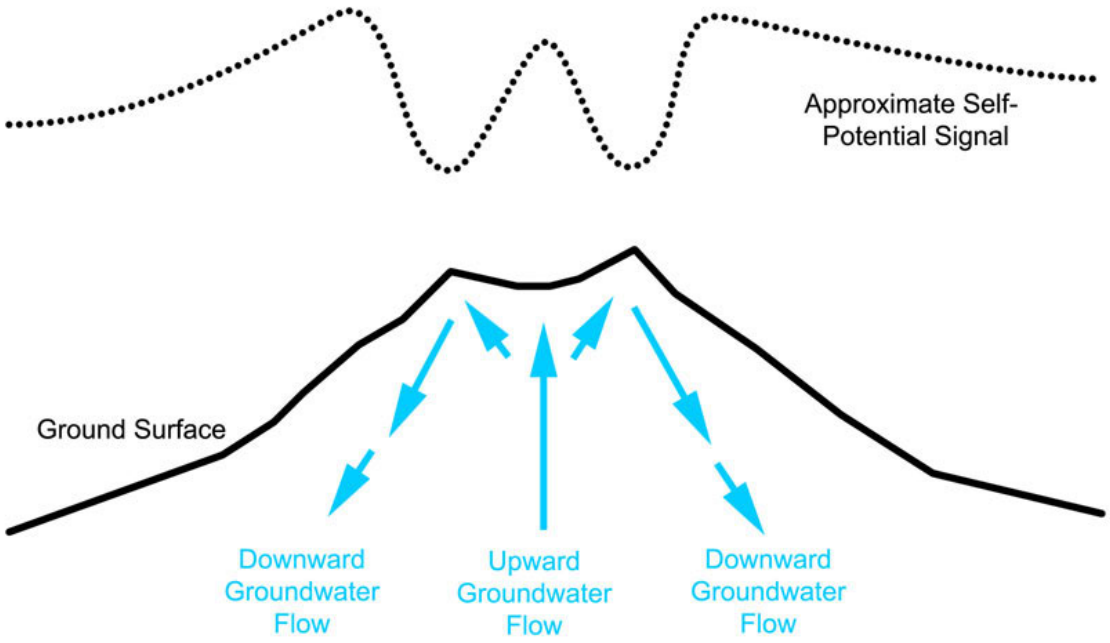

Figure 1.1. Illustration of the general shape of a self-potential anomaly over a volcano. Modified from Michel and Zlotnicki, 1998.

Kilauea over known fumarolic areas and recent fissures (Zablocki, 1976), but no anomalies were detected on Etna over fumaroles or shallow fissures, instead only over deeper fissures (Massenet and Pham, 1985). On several volcanoes, such as Aso (Japan) (Hase et al., 2005) and Piton de la Fournaise, the self-potential signal is mainly positive as water upwells from below, with downward flow driven by topography while other volcanoes, i.e. Vulcano (Barde-Cabusson et al., 2009) and Misti (Finizola et al., 2004), exhibit extreme negative anomalies on the flanks that do not correspond directly to topography.

The volcano of interest in this study is Mount St. Helens, a dacitic stratovolcano in the Cascade range in Washington state. After a major flank collapse on Mount St. Helens in 1980, nearly 450 m of elevation was removed from the volcano. The removal of the north face of the volcano allows an insight into the deeper plumbing of the volcano. Also,

periodic dome-building eruptions allow further insight into the development of a new hydrothermal system following a catastrophic eruption.

Self-potential measurements were taken on Mount St. Helens in 2000 and 2001, over a decade after the end of the first major dome-building eruption from 1980 to 1986. Results of this survey revealed a large negative anomaly (-1300 mV) on the north flank of the 1980-86 dome. Figure 1.2. displays data from the survey from Bedrosian et al. (2007) that shows the basic shape and size of the large negative anomaly in question. Bedrosian et al. (2007) concluded that the correlation between topography and self-potential between 0 and 2000 m is likely of hydrothermal origin, and that the anomaly's radial symmetry is indicative of a dome-scale anomaly.

Bedrosian et al. (2007) proposed that a possible conduit for downward flow was a fault scarp formed during the 1980 eruption. Chadwick and Swanson (1989) describe the scarp as a large thrust fault striking approximately east-west, and dipping to the north.

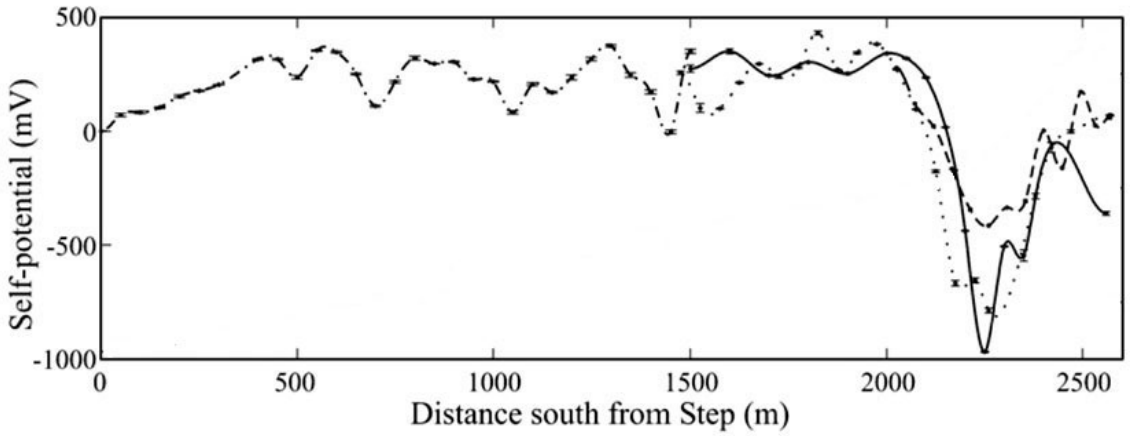

Figure 1.2. Self-potential data collected in 2000 and 2001 on Mount St. Helens. Different line types indicate different paths up the volcano. Modified from Bedrosian et al. (2007).

Eventually, the scarp was buried by the 1980-86 lava dome. An alternative cause of the anomaly also proposed in Bedrosian et al. (2007) is that downward flow is channeled along boundaries of past extrusions.

The main focus of this study is another self-potential survey that was conducted in 2007, near the end of a second dome-building eruption. One objective was to expand the coverage from the previous survey in the crater floor as well as on the 1980-86 dome. Another objective was to study the change in the behavior of the hydrothermal system following a dome-building eruption and to understand the plumbing of the hydrothermal cell.

Time-domain electromagnetics collected during the 2007 survey were one-dimensionally inverted for a four-layer resistivity model on the crater floor by Bedrosian et al. (2008). This information was integrated with self-potential measurements near the dome and allowed the creation of a simple hydrogeologic model for groundwater flow on the north side of Mount St. Helens. Lack of resistivity data near the dome prevented inversion of the self-potential for Darcy velocity, so instead a flexible forward model was created based on the hydrogeologic model. Forward modeling of self-potential on volcanoes has been done by Gerstnecker et al. (2004), Ishido (2004), Revil et al. (2008), and Aizawa et al. (2009). The model presented in Aizawa et al. (2009) was used as the basis for the forward model of Mount St. Helens in COMSOL Multiphysics® 3.5. The modeled self-potential signal was then compared to the data collected in 2000, 2001, and 2007 to illustrate the plausibility of the hydrogeologic model.

CHAPTER 2
GEOLOGIC HISTORY OF MOUNT ST. HELENS

Mount St. Helens is a young dacitic stratovolcano located in southwestern Washington State. It is one of many volcanoes that line the United States' west coast as part of the Cascades Mountain Range, formed by the subduction of the Juan de Fuca plate beneath the North America plate. Its location with respect to the rest of the Cascade Range volcanoes is shown in Figure 2.1. Of these volcanoes, Mount St. Helens is the most active, with more than 14 known eruptions in the last 4,000 years (Ewert et al., 1994). These eruptions range in scale from small ash and debris flows to the catastrophic lateral blast and Plinian eruption of May 18, 1980 (Tilling et al., 1990).

This chapter describes the history of Mount St. Helens before 1980, the major events of the 1980 eruption, and the activity of the volcano after 1980.

2.1 History Prior to 1980 Eruption

The evolution of Mount St. Helens in the last 300,000 years can be described in four main stages of eruptive activity characterized by long periods of dome building followed by quiescence: Ape Canyon Stage (300-35 ka), Cougar Stage (28-18 ka), Swift Creek Stage (16-12.8 ka), and Spirit Lake Stage (3.9-0 ka) (Clynne et al., 2008). The Spirit Lake stage is of most interest, and can be further subdivided into seven periods. The oldest period, Smith Creek Period (3.9-3.3 ka), was defined by two large ash eruptions, the second of which is estimated to have erupted four times more ash than the 1980 eruption. The second period, Pine Creek Period (2.9-2.55 ka), was mostly characterized by repeated collapse of growing lava domes clustered around the future summit. Debris

Figure 2.1. Location map of Mount St. Helens and other Cascade Range volcanoes. From (Tilling et al., 1990), courtesy U. S. Geological Survey.

fans from these collapses are estimated to be as much as 600 meters thick on the south flank. During the Castle Creek Period (2.55-1.895 ka), several layers of lava flows, ranging from basaltic to dacitic in nature, flowed down the slopes of the evolving mountain. The Sugar Bowl Period (A.D. 900-850) produced three small domes on the western flank of the volcano. The pre-1980 summit dome was emplaced during the late Kalama Period (A.D. 1479-1720), and a small dome on the north flank was created

during the Goat Rocks Period (A.D. 1800-1857). The erupted materials to this point comprised the pre-1980 edifice. Mount St. Helens is currently considered to be in its Modern Period, and this includes the events from A.D. 1980 to present (Clynne et al., 2005).

2.2 May 18, 1980 Flank Collapse and Plinian Eruption

Mt. St. Helens is perhaps most well-known for the lateral blast and accompanying Plinian eruption of May 18, 1980. In the months preceding the main event, more than 10,000 small earthquakes (many above M 2.6) were recorded, including a M 4.2 earthquake on March 20, 1980. These earthquakes were localized less than 2.6 km beneath a large bulge that began forming on the north face of the volcano (Tilling et al., 1990).

On May 18, a M 5.1 earthquake triggered the collapse of the north flank of the volcano where the bulge was forming. This collapse in turn triggered a large lateral blast to the north and created a vertical eruption column that reached 24 km in height (Brantley and Myers, 2000). The lateral blast completely destroyed the north face of the volcano, creating a large, asymmetrical crater open toward the north. Several pyroclastic flows and a large lahar were also produced that day. In the days and months to follow, more debris, ashes, and pyroclastic flows were deposited on the breach (the region on the north face exposed by the lateral blast), the total thickness of which are estimated to be 36 meters deep in some places (Brantley and Myers, 2000). Figure 2.2 illustrates the extreme difference in the shape of the volcano from before the 1980 eruption to a few months after.

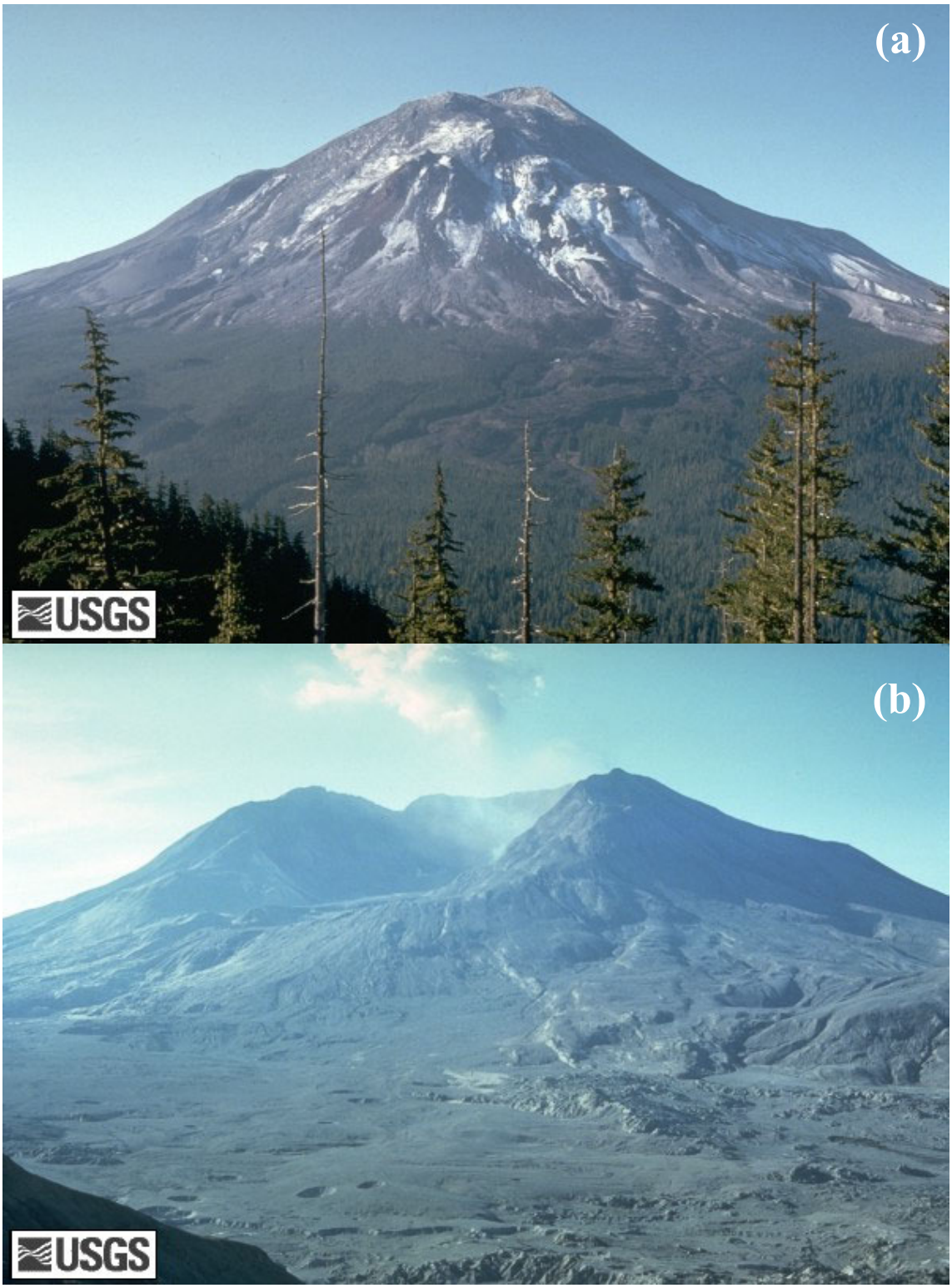

Figure 2.2. Photographs of Mount St. Helens from Johnston Ridge, approximately 8 km to the north-northwest. At left, (a) pictures Mount St. Helens on May 17, 1980, the day before the eruption. At right, (b) pictures Mount St. Helens on September 10, 1980, after the eruption. Photographs by Harry Glicken, USGS.

2.3 Post-1980 Dome Building Eruptions

A major part of a volcano's evolution is the extrusion of lava to create domes. As mentioned in Section 2.1, Mount St. Helens has undergone numerous dome-building eruptions. Two such eruptions occurred after the 1980 collapse, the first beginning in 1980, and the second in 2004. From October 1980 to October 1986, a dacite (silica rich) lava dome was extruded in the center of the 1980 crater over the course of 17 eruptive periods. The dome towered 267 meters above the 1980 crater floor and had a width of over one kilometer (Brantley and Myers, 2000). This dome is referred to hereafter as the "1980-86 Dome."

Mount St. Helens then entered dormancy with intermittent but minor eruptive activity. Schilling et al. (2004) report that during this time a large, horseshoe shaped glacier began to form between the 1980-86 dome and the crater wall. As the crater began to cool, snow began to build up during the winter and was then overlain by periodic rockfall from the crater walls. The Crater (or Amphitheater) Glacier is estimated to be 200 meters thick in some areas (Schilling et al., 2004).

In September 2004, Mount St. Helens began to extrude lava again. However, instead of extruding lava in the same place as in 1980, a new dome began forming to the south of the 1980-86 dome, beneath the Crater Glacier (Major et al., 2005). Lava extrusion continued until January 2008, and a new dome of nearly the same volume of lava as in 1980 to 1986 was formed (Topinka, 2008). The formation of the "new" dome caused the Crater Glacier to be considerably deformed. Figure 2.3 illustrates the changes in the topography of the volcano in the vicinity of the lava domes from late 2003 to early 2006.

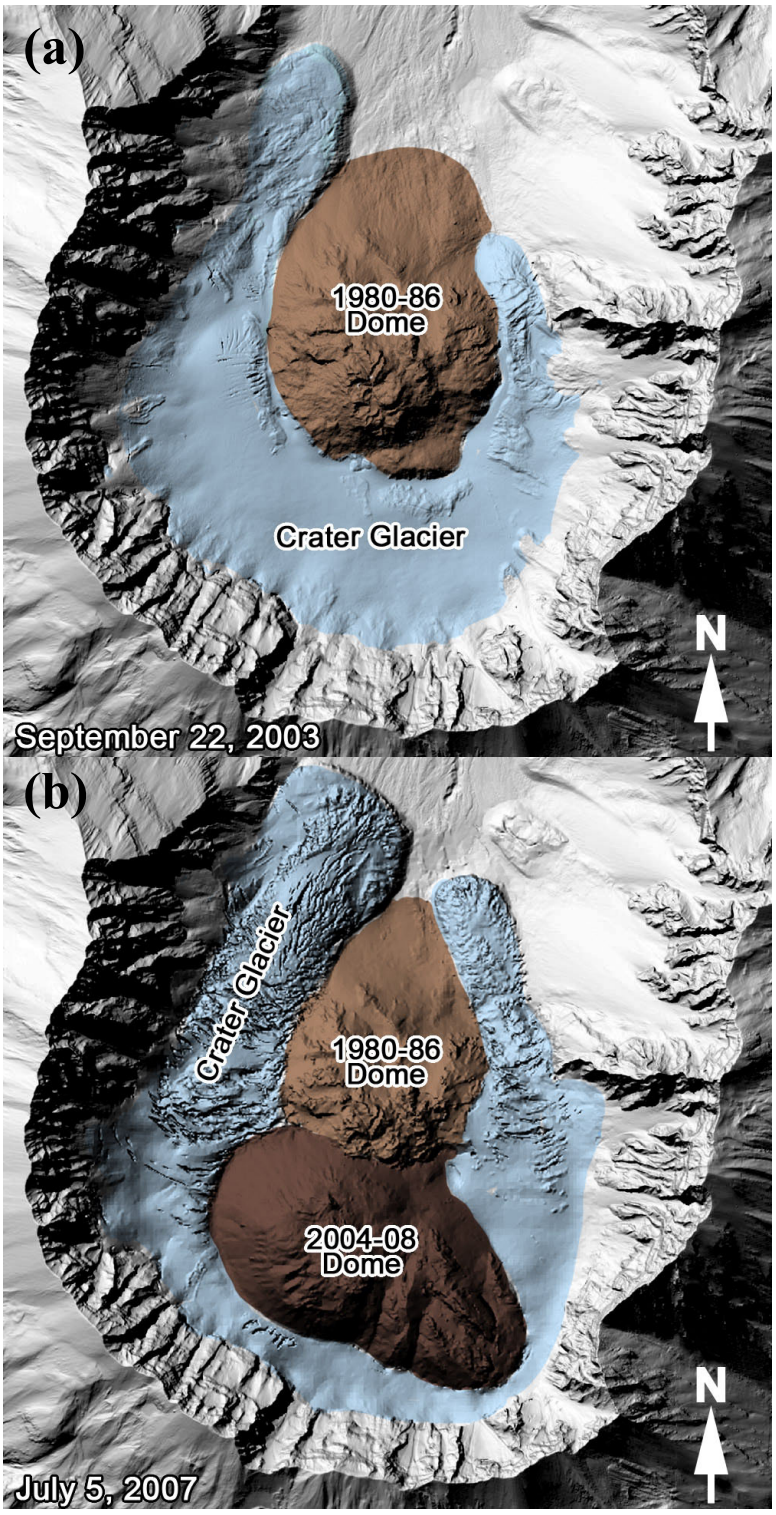

Figure 2.3. Digital Elevation Models (DEMs) of Mount St. Helens. (a) is from September 22, 2003 and notes the location of the Crater Glacier and the 1980-86 dome. (b) is from February 9, 2006. The new dome is located to the south of the 1980-86 dome, and the Crater Glacier has been deformed and moved northward to accommodate growth of the new dome. Modified from Messerich et al. (2008).

CHAPTER 3
SELF-POTENTIAL METHOD

Self-potential (SP) is a naturally occurring phenomenon where electric potentials are created by various sources such as redox reactions and groundwater flow. Self-potential signals are passively recorded electrical potentials measured using two non-polarizing electrodes, a length of insulated wire, and a high impedance (>10 MΩ) voltmeter. The light weight of the equipment and the sensitivity to groundwater flow make self-potential a useful geophysical method to study hydrothermal systems on volcanic terrain. This chapter describes the various causes of self-potential and its applications to geothermal systems.

3.1 Sources of Self-Potential

After its discovery in 1830 (Fox, 1830), self-potential has mainly been used in the prospection of ore bodies. The self-potential produced in this case is related to the corrosion of the ore body and the subsequent creation of a redox potential (Castermant et al., 2008). Redox potentials can also be created by contaminant plumes, but such applications are outside the scope of this paper (Nyquist and Corry, 2002; Naudet et al., 2003).

Thermoelectric potential is another source of self-potential often observed in areas of geothermal activity. This phenomenon arises from the Soret effect, where ions diffuse with different mobilities through pores due to a thermal gradient. Typically the coupling coefficient is on the order of 1 mV/ºC. Thermoelectric effects can produce anomalies of up to 200 mV in the presence of extreme thermal gradients (Corwin and Hoover, 1979).

The main source of self-potential I will discuss is the streaming potential caused by the flow of water through porous media. Streaming potential can be explained using an electrical double-layer model, shown in Figure 3.1. In this model, there is an excess of charge at the pore wall because of the chemical reactivity of the mineral surface with the pore water. The fixed charge on the mineral surface is counterbalanced by a charge located in the pore water in the vicinity of the mineral surface. It follows that the pore water within an electrical diffuse layer close to the surface has a net charge density.

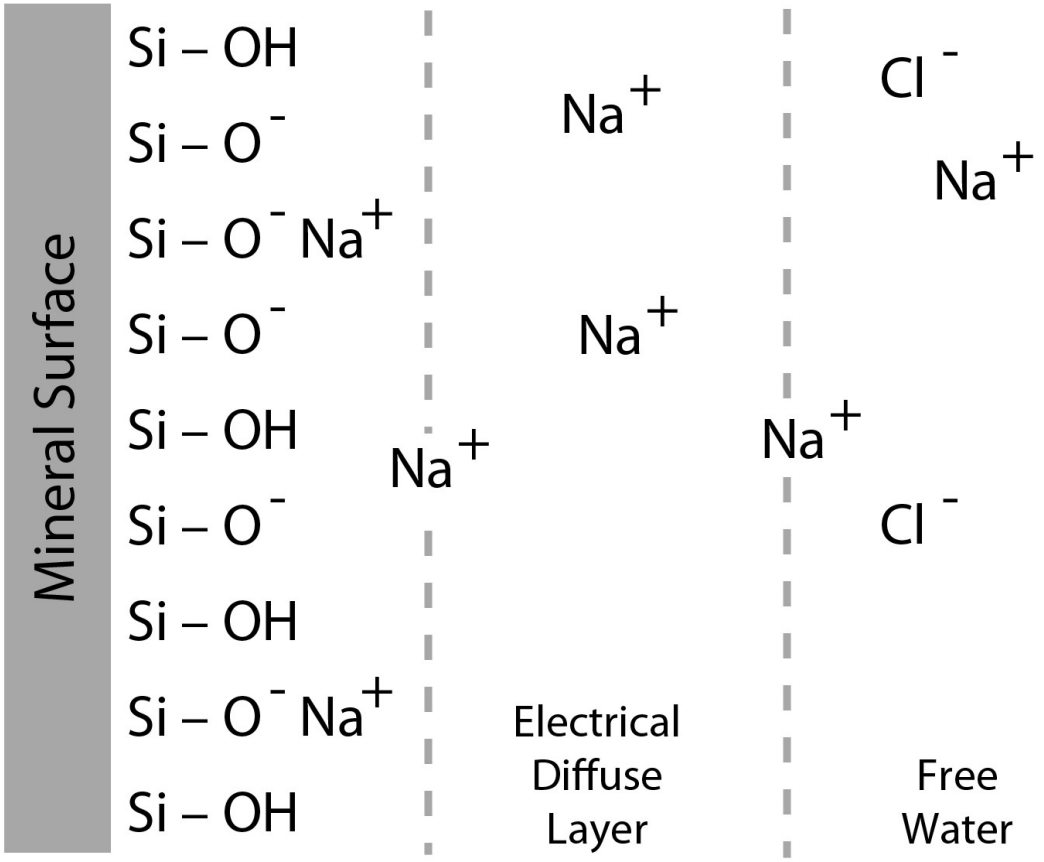

Figure 3.1. Electrical double-layer model. The electrical diffuse layer represents excess ions attracted to the charged mineral surface. Free water is the electrically neutral water in the pore. Note that the total volume is electrically neutral. Modified from Revil et al. (1999).

Therefore the flow of the pore water carries a net electrical charge. This creates a convective current density (Sill, 1983; Revil et al., 1999).

Revil and Linde (2006) used volume averaging to show that the source current density $\vec{j}_s$ (A/m^2) created by the drag of the excess of charge in the diffuse layer by the flow of the pore water can be defined as:

$$\vec{j}_s = \overline{Q}_v \vec{u} \tag{3.1}$$

where $\overline{Q}_v$ is the volume average of the excess charge of the diffuse layer (C/m^3), and $\vec{u}$ is the Darcy velocity of the seepage of the water (m/s). The total current density, $\vec{j}$ (A/m), is:

$$\vec{j} = \sigma \vec{E} + \vec{j}_s \tag{3.2}$$

where σ is the conductivity (S/m), and $\vec{E}$ is the electric field (V/m). The first term of Eq. (3.2) is a conduction current density as defined by Ohm's law. The electric field is related to voltage, φ (V), simply by:

$$\vec{E} = -\nabla \varphi \tag{3.3}$$

in the quasistatic limit of the Maxwell equations so the curl of $\vec{E}$ is zero. In addition to the previous constitutive equations, we need to add a continuity equation for the charge:

$$\nabla \cdot \vec{j} = 0 \tag{3.4}$$

Substituting equations 3.2 and 3.3 into equation 3.4 reveals that the governing equation for self-potential is in the form of a Poisson's equation,

$$\overline{Q}_v \nabla \cdot \vec{u} - \sigma \nabla^2 \varphi = 0 \tag{3.5}$$

which can be solved using finite differences. The self-potential produced by a given distribution of groundwater flow and conductivity structure can be solved for using finite element modeling. At the surface, we measure voltages produced by self-potential, and

conductivity structure can be determined from a range of methods, such as direct current (DC) resistivity measurements or from time domain electromagnetic (TDEM) measurements. Determining $\overline{Q}_v$ usually involves laboratory measurements of samples, but it can be inferred from permeability (Jardani et al., 2007).

In general, the conductivity structure and the self-potential are measured, and the causative groundwater flow is unknown and the parameter of interest. Therefore, given a conductivity structure and a distribution of self-potential measurements at the surface or down a borehole, it is possible to solve for the source electrical current density (Minsley et al., 2007) or directly for the Darcy velocity of groundwater flow via inversion (Jardani et al., 2006; Jardani et al., 2007). However, in the case of forward modeling discussed in Chapter 6, if one wishes to solve for self-potential instead, the electrical conductivity structure and excess charge must be known and the Darcy velocity assumed.

3.2 Application of Self-Potential to Geothermal and Volcanic Systems

Self-potential is well-suited to applications in geothermally active areas because large potentials can be caused by the circulation of water in a hydrothermal convection cell. It has been shown that as water rises, it creates a positive potential anomaly at the surface and as it moves downward, a negative anomaly (Revil et al., 1999; Poldini, 1938). Self-potential measurements have been performed on several geothermal fields in Idaho, Nevada, and Mexico, each with distinct dipolar anomalies on the order of tens to hundreds of mV (Corwin and Hoover, 1979).

On volcanoes, the amplitude of the self-potential anomaly is much higher than in other geothermal areas, and can be on the order of several volts. For example, a 1 V anomaly was detected on Mount Unzen (Hashimoto and Tanaka, 1995), 1.5 to 2 V

anomalies were detected on Iwate, Nantai, and Nikko-Shirane volcanoes (Aizawa et al., 2009), and a 2.5 V anomaly was detected on Mount Fuji (Aizawa et al., 2005). In all cases, a positive anomaly was detected at the summit of the volcano, and a large negative anomaly was detected on the flank. In most cases, the anomaly was very broad (on the order of several hundred meters to kilometers) and asymmetric.

In addition to mapping self-potential at a single point in time to study its shape, repeated self-potential measurements have been used on volcanoes to study pre-eruptive and post-eruptive changes in the hydrothermal system. On Mt. Unzen, there was a rapid increase in self-potential in the months preceding the first extrusion of lava (Hashimoto and Tanaka, 1995). Self-potential has also been shown to correlate to ultra-long-period seismic signals on volcanoes in periods before their eruption (Sasai et al., 2002; Byrdina et al., 2003). Repeated mapping surveys over a span of 20 years on Piton de la Fournaise volcano has revealed a constant hydrothermal system, with smaller positive anomalies appearing during volcanic activity (Michel and Zlotnicki, 1998), and repeated surveys on Mt. Usu (Japan) documented the growth of a new geothermal field (Saba et al., 2007).

CHAPTER 4
FIELD MEASUREMENTS ON MOUNT ST. HELENS

Mount St. Helens is extensively monitored by the U. S. Geological Survey Cascades Volcano Observatory (USGS-CVO) in terms of earthquake seismicity, gas emissions, geologic mapping, thermal output, ground deformation, and more (Ewert et al., 1994). However, the danger associated with working on an active and unstable volcano combined with its inaccessibility mean that ground-based geophysical surveys are difficult. Even though self-potential is well-suited to volcanic studies, only four small self-potential surveys have been done on Mount St. Helens. This chapter describes the main August 2007 survey, and the three surveys completed before then.

4.1 Previous Surveys

Several self-potential studies have been undertaken on Mount St. Helens since it erupted in 1980. The first study consisted of a continuous monitoring of the self-potential on the east flank of the volcano, beginning in September 1980 and lasting two years. Significant temporal changes were measured in October 1980, but it was not determined whether the changes were due to volcanic activity or rainwater flowing over the electrodes (Davis et al., 1989).

A large-scale self-potential survey on Mount St. Helens was carried out in 1982 to the north of the forming dome. A positive self-potential anomaly was recorded in the vicinity of the dome and along the axis of the breach to the north, and a negative, east-west trending anomaly was recorded near the rampart, a step in topography approximately 1 km north of the dome associated with a possible structural weakness (Anderson et al., 1983; Bedrosian et al., 2007).

During the lull in volcanic activity, two more self-potential surveys were conducted in August 2000 and September 2001. Measurements were taken every 50 m along four main profiles, the longest of which extended 2.5 km from the top of Step Falls to within 100 m of the 1980-86 dome summit. A large, ~1.5 V negative anomaly was measured at the base of the dome, followed by a positive anomaly closer to the summit.

The anomalies in both cases were attributed to the existence of a hydrothermal cell centered beneath the 1980-86 dome (Bedrosian et al., 2007). Figure 4.1 is an illustration from Bedrosian et al. (2007) that is one possible explanation for the dipolar anomaly seen on the dome. In this model, water is exsolved from the magma as it cools and is cycled into the hydrothermal cell from below. Water is also introduced into the system by rainfall, which on Mount St. Helens is approximately 140 inches per year, precipitated almost entirely in the winter months (Tilling et al., 1990), as well as from glacial melt. The water in the system is heated from below by magma and rises toward the surface, then sinks back into the system as it cools.

4.2 August 2007 Survey

When Mount St. Helens began erupting again in 2004, field surveys in the crater of more than a day were not possible because the risk was too high. By 2007, the eruption's intensity had decreased significantly, and a two-week long survey was possible. This survey, completed between July 23 and August 4, 2007, focused primarily on repeating as many points from the 2000-2001 survey as possible, as well as collecting time domain electromagnetic measurements to aid in constraining resistivity structure.

Figure 4.2 shows the basic setup of the self-potential survey. At each 'base' station, a computer was connected to a high impedance (10 MΩ) voltmeter via USB connection,

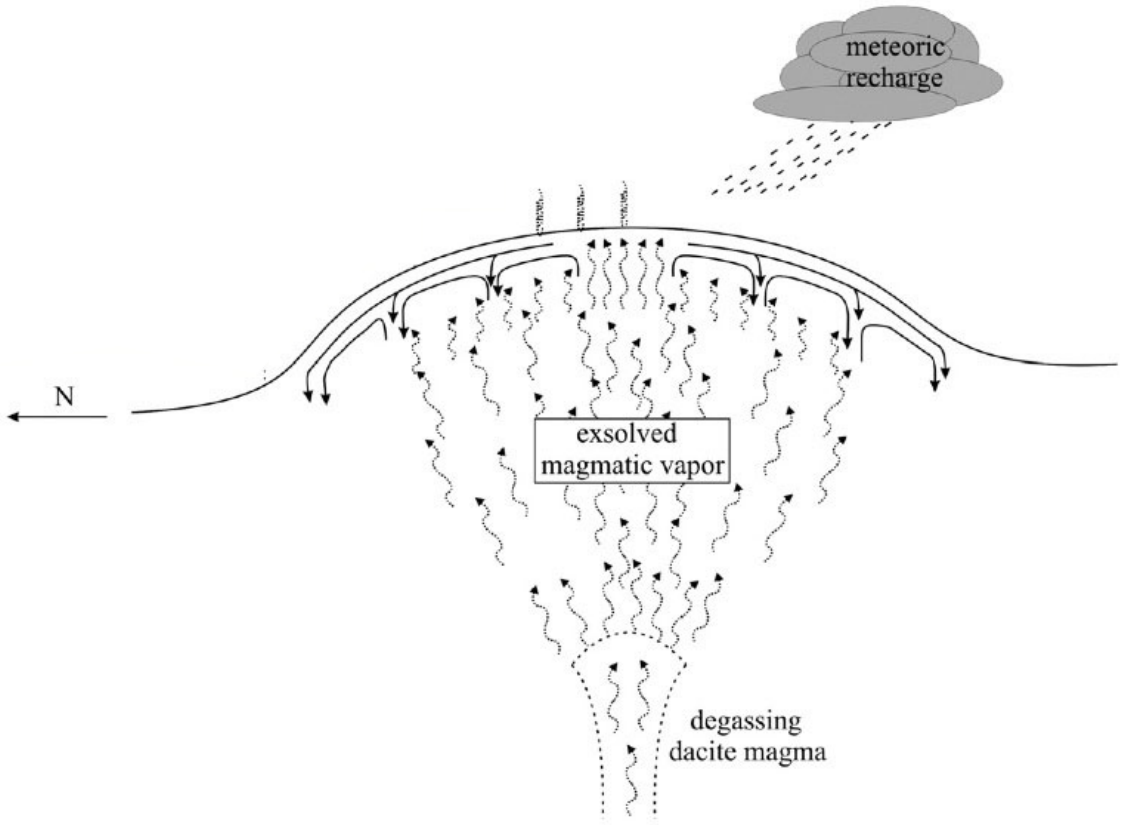

Figure 4.1. Inferred hydrothermal circulation within the dome from Bedrosian et al. (2007). Water is introduced into the system by cooling magma and meteoric inflow, rises as it is heated from below, and percolates back into the system as it cools.

and the negative terminal of the voltmeter was connected to a stationary electrode buried a few centimeters deep next to the computer. The positive terminal was connected to a 500 m reel of wire, which was then connected to the roving electrode. The roving electrode was transported in a small bucket with a dampened sponge at the bottom to keep the electrode wet. Four small holes were dug with a hand tiller in a one meter square area around each measurement point to enhance contact with the ground and to assess data variability. Data were collected for five seconds, with one measurement per second, in each hole. Measurements were taken every 50 m out to as far as either topography or the length of the wire would allow, and then the base station was moved to a new

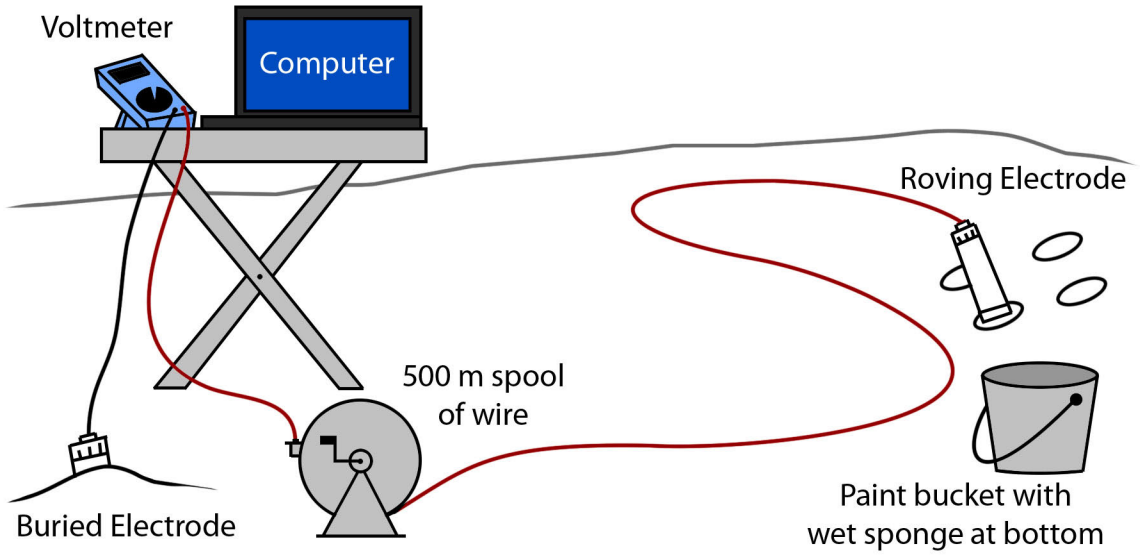

Figure 4.2. Basic self-potential field setup. A computer is attached to a high-impedence voltmeter, which is then attached to two non-polarizing electrodes. One elctrode is buried near the base station, and the other is a roving electrode attached to a 500 m spool of wire and transported in a bucket with a sponge and saline solution in the bottom.

location. In total, there were three separate base locations, and points at the ends of each survey were duplicated to allow each section to be tied back to one reference point.

For this survey, we used non-polarizing Pb-$PbCl_2$ electrodes made of PVC pipe and a porous wooden cap made by John Booker of the University of Washington. The electrodes have a very small temperature dependence, on the order of 20 µV/ºC at a pH between 4 and 5 (Petiau, 2000). To check electrode polarization, at the beginning of each line we placed the electrodes together in a salt-water solution and recorded the voltage between the electrodes. Once a line was complete, we repeated the process. Over the course of a few hours, the roving electrode would heat up and begin to polarize compared with the stationary electrode, but at most we recorded a polarization of -1.9 mV over 1.5 hours. Assuming that the drift was linear with respect to time, a simple correction could be applied to the measurements after the survey was complete.

Another source of error to consider in self-potential measurements is the effect of telluric currents. During the 2000-2001 survey, it was determined that the effect of telluric currents was negligible over the time scale of the survey by using a stationary dipole and monitoring the response over two days (Bedrosian et al., 2007). We assumed during the 2007 survey that this was also the case.

Measurements were taken every 50 m along an approximately north-south line. Two lines were measured to the north of the rampart, a grid was set up south of the rampart, and measurements were taken on accessible areas on the 1980-86 dome. Figure 4.3 is a map of the locations where self-potential was measured in 2007 compared to 2000-2001. Locations for the 2007 survey were determined using GPS locations of two main stations from the 2000-2001 survey, one near the base of the rampart, and the other near Loowit creek. From these points, a 50 m grid was set up using a laser distance meter, and a brunton. The extent of the survey was severely limited by topography associated with Step and Loowit creeks, the rampart, and the Amphitheater glacier. Note that several of the 2000-2001 measurement locations are buried by the Amphitheater glacier.

Time-domain electromagnetic measurements were taken on the crater floor in association with the locations of self-potential measurements using a Zonge GDP-32 system. Figure 4.4 is a map of the locations of the TDEM loops with respect to nearby self-potential measurements. Each loop was 50 meters square, and measurements of the z-component of the secondary magnetic field were acquired in the center of each loop. Unfortunately, the furthest south the measurements extend is only to the base of the 1980-86 dome. TDEM measurements further south than this were too difficult to acquire because the extreme topography of the dome prohibited laying out extended loops.

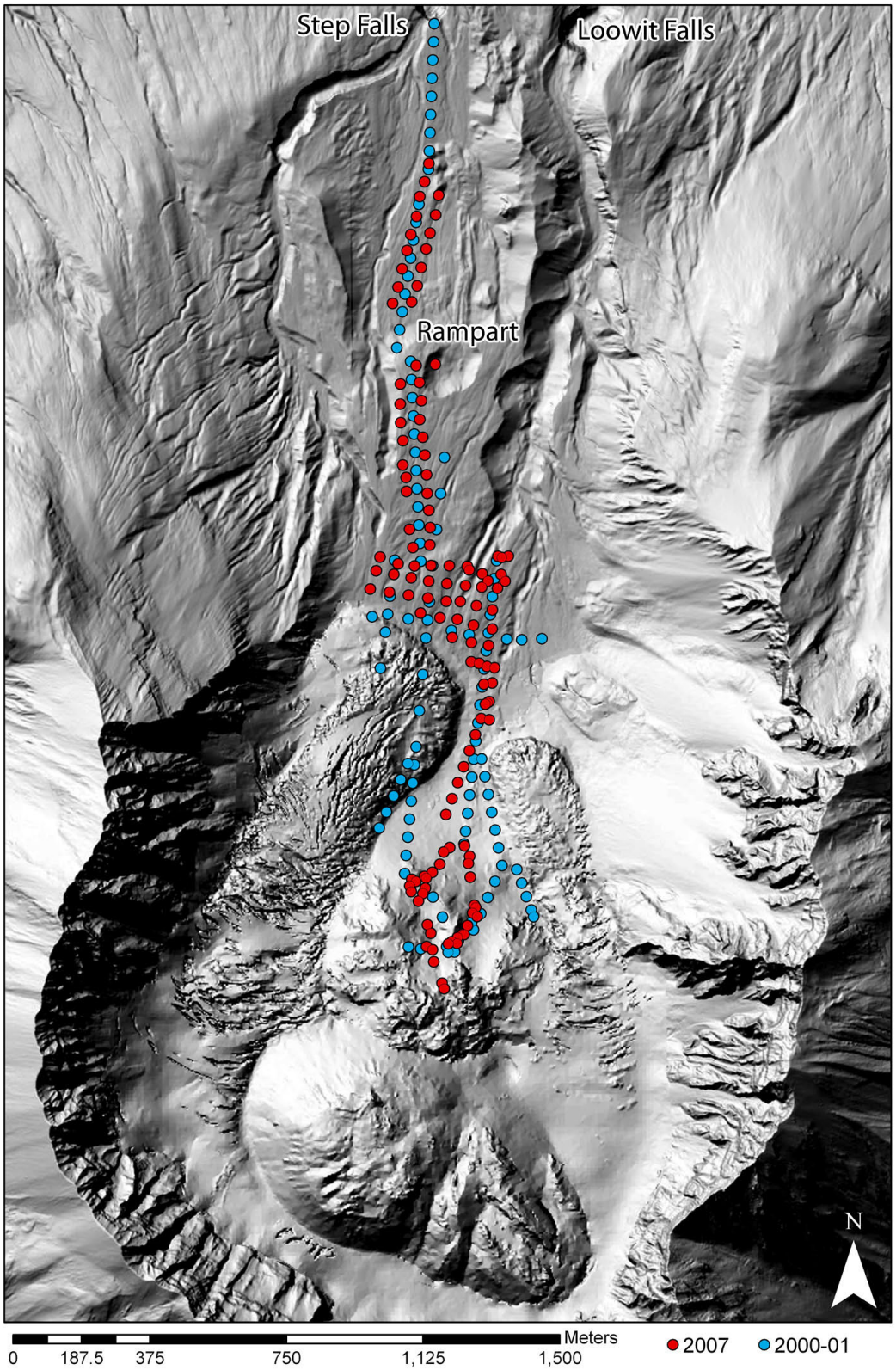

Figure 4.3. Location map of self-potential measurements on 2007 digital elevation model, with older measurements in blue, and newer measurements in red. Several of the 2000-01 measurements were buried by advance of the glacier and could not be repeated.

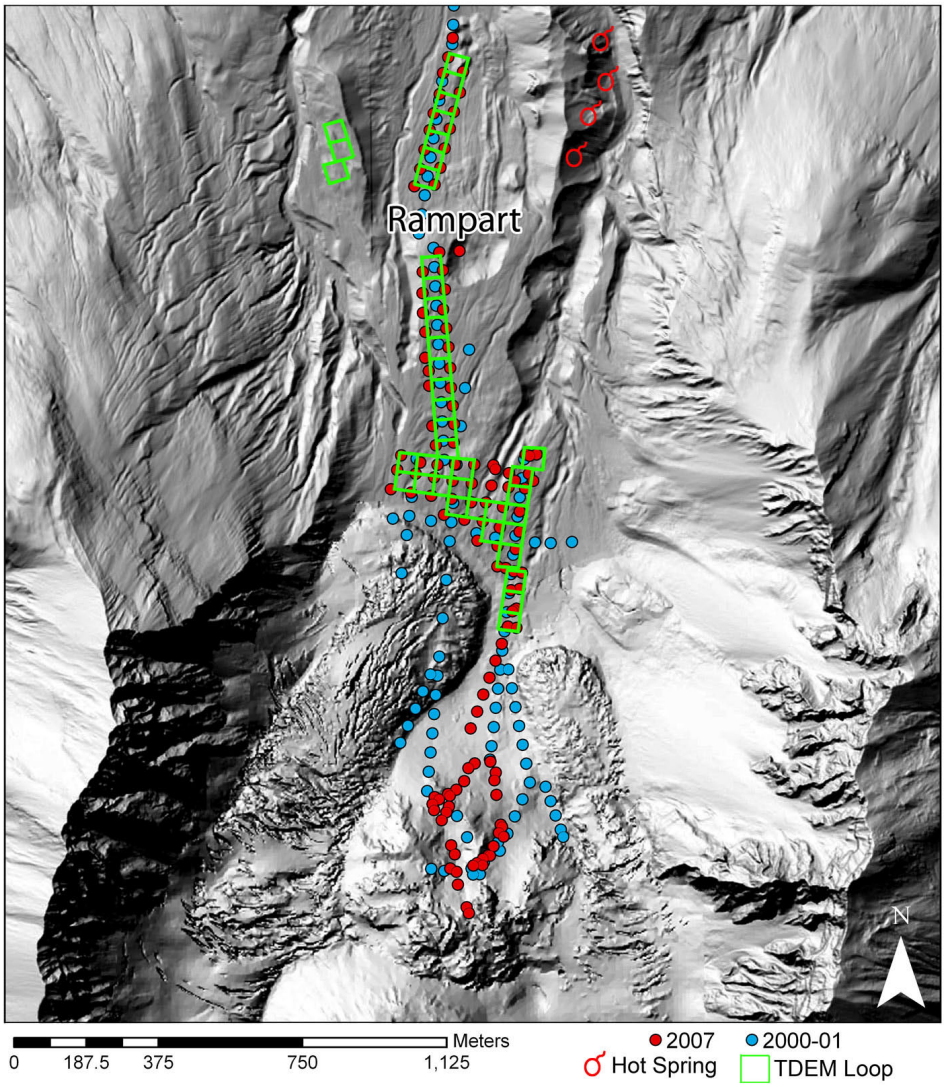

Figure 4.4. Locations of TDEM measurements (green loops are wires, measurements taken at the center of each loop) with respect to nearby self-potential measurements, nearby hot springs, and the rampart. Spatial coverage only extends to the base of the 1980-86 dome.

CHAPTER 5
DATA PROCESSING AND INTERPRETATION

Once the survey was completed, minimal processing needed to be done on the data. This chapter describes the processing of the August 2007 self-potential survey, and compares the results to the 2000-2001 survey. The results are then compared to the results of the TDEM survey, and a possible model for groundwater flow is presented.

5.1 Processing of Self-Potential Data

Processing for the August 2007 survey was carried out as closely as possible to the processing described in Bedrosian et al. (2007) so that the two datasets could be compared. First, a drift correction for the polarization of the electrodes was applied. A linear function of drift vs. time was created from two polarization checks, one at the beginning of the survey and one at the end. An independent drift function was calculated for each line collected. The data logger program for the voltmeter recorded the time that each data point was collected, and this time was substituted into the drift function to solve for drift. The calculated drift was then subtracted from each individual measurement, which in general was never more than 1 mV of drift per hour.

Once the data had been corrected for drift, the self-potential at each location needed to be determined. Each location was associated with 20 measurements (5 measurements in 4 nearby holes). Usually, an average (arithmetic mean) of all the points was calculated, followed by a calculation of the standard deviation. However, sometimes there were obvious outliers in the data where measurements in one of the four holes varied significantly from the other three. If these measurements were outside two standard

deviations of the other data points, the hole was discarded and a new average was computed using only 15 data points.

The next step was to reference the potential at all points back to a single point. I chose the northernmost point from the 2007 survey nearest Step Falls as the reference point. The value of potential at this point, named "n1100" for its distance north from the initial base station, was subtracted from each location that shared its original reference point. Repeat measurements at the same point with reference to two different reference points were set to the same potential, and the difference was subtracted from each other point using the same reference. A source of error arises here if the potential changes at the tie points from one survey to the next. For simplicity, I assume that the potential at a single point did not vary significantly with time.

Even though all the points were now referenced back to the same point, there were still some duplicate measurements. These points were averaged together using a weighted average, using the number of holes as the weight.

5.2 Comparison to 2000-2001 Self-Potential Data

One of the main goals of the 2007 survey was to compare the new data with the data acquired in 2000-2001. Paul Bedrosian provided me with the processed 2000-2001 dataset in order to accomplish this. One minor problem was that 2000-2001 dataset was referenced back to a different point (further north) than the 2007 dataset. Both datasets shared one common point ("B2"), and I used this point to reference the 2000-2001 dataset to the 2007 dataset by subtracting the difference from all points in the older dataset. Again, I assumed that the potential at this point did not vary over a six year period as it was located far from the dome and most changes associated with eruptive

activity. Now that the two datasets were referenced back to a single point, I could compare the two side by side. Figure 5.1 shows the results of both datasets, with distance set as the absolute distance from n1100. In this case, I assume that the data were collected in enough of a straight line that absolute distance is a decent approximation of a north-south trending line from the bottom of the crater floor to the top of the 1980-86 dome. Also, a 10^{th} order polynomial trendline has been overlaid on the data to loosely highlight the basic trend of both datasets, and was chosen for smoothness without over-fitting the data. However, the trendline does not incorporate several of the interesting aspects of the data such as the downward trend of the 2007 dataset past 2000 m distance.

The two datasets exhibit striking resemblance, with the same approximate value on the crater floor between 0 and 1500 m, a similar drop in potential between 1500 and 2000 m, and an increase in potential from 2000 m toward the top of the dome. Perhaps the largest difference is the amplitude of the negative anomaly between 2000-2001 and 2007. In 2007, the largest negative anomaly reaches only -700 mV, whereas the negative anomaly in 2000-2001 reaches -1300 mV. However, it should be noted that the negative anomalies do not align spatially.

Another curiosity is the downward trend of the 2000-2001 dataset northward from 0 m to -500 m. Unfortunately, the extent of the 2007 dataset is not this far north, and the cause of this trend is uncertain. There is a slight change in topography north from 0 m approaching Step Falls, but it is not substantial compared to the rest of the topography.

An interesting aspect of the data is the spread in the values of its points. On the crater floor, the data center near 0 mV, perhaps even with a slight positive trend, but spread over 150 mV in either direction. Part of the spread has to do with the fact that

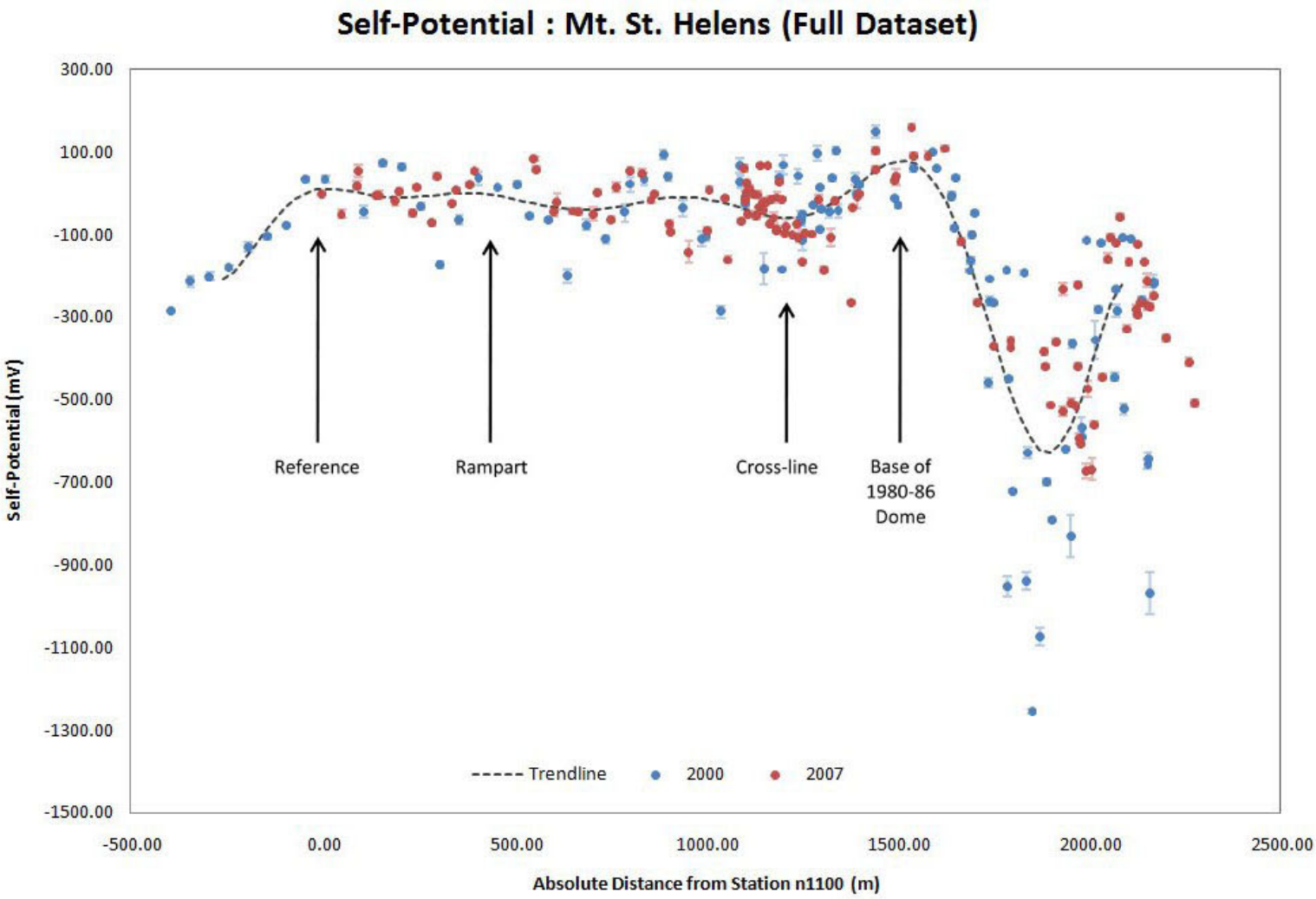

Figure 5.1. Full dataset of self-potential data from 2000-2001 and 2007 with reference to northernmost point in 2007 (n1100) and plotted against absolute distance. Trendline is a 10th order polynomial fit to both datasets. Major landmarks are noted.

several parallel lines are projected onto the same graph, but this is not the case for the 2000-01 dataset where between 0 and 2000 m there is only one line. Also, the individual data points were highly repeatable, so noise in the data collection is not to blame either. It seems that the self-potential signal is very sensitive to heterogeneity in the subsurface, especially on the crater floor where flow is less driven by the hydrothermal system.

Although there does appear to be a decent amount of spread in the data near the dome, most of the data on the crater floor are tightly clustered so the assumption that the anomaly is essentially two-dimensional is probably a decent one. To better visualize and compare the data, I reduced the data down to two main lines on the crater floor, one line for each survey, and then four lines on the dome. Figure 5.2 is a map of the lines chosen for the comparison. Essentially, two main lines of data were collected in 2007, and these corresponded spatially to two lines collected in 2000 and 2001.

Figure 5.3 is a graph of the self-potential measurements carried out on the lines from Figure 5.2. Unlike Figure 5.1, the data points are smoothly interpolated with a piecewise function that, because it follows along individual lines, more accurately portrays trends in the data. From about 0 to 1600 m from the reference, the two datasets are generally similar, with highs and lows of similar amplitude in approximately the same places. Past 1600 m, however, the two datasets begin to diverge. In the 2000-01 dataset, the two lines on the dome have minima at approximately 1800 m, of -1100 and -700 mV each. In the 2007 dataset, one of the lines has a minimum at 2000 m from the reference of -700 mV, and the second line decreases slightly but then turns upward after 1800 m. In fact, the two lines almost appear to be mirror images of each other.

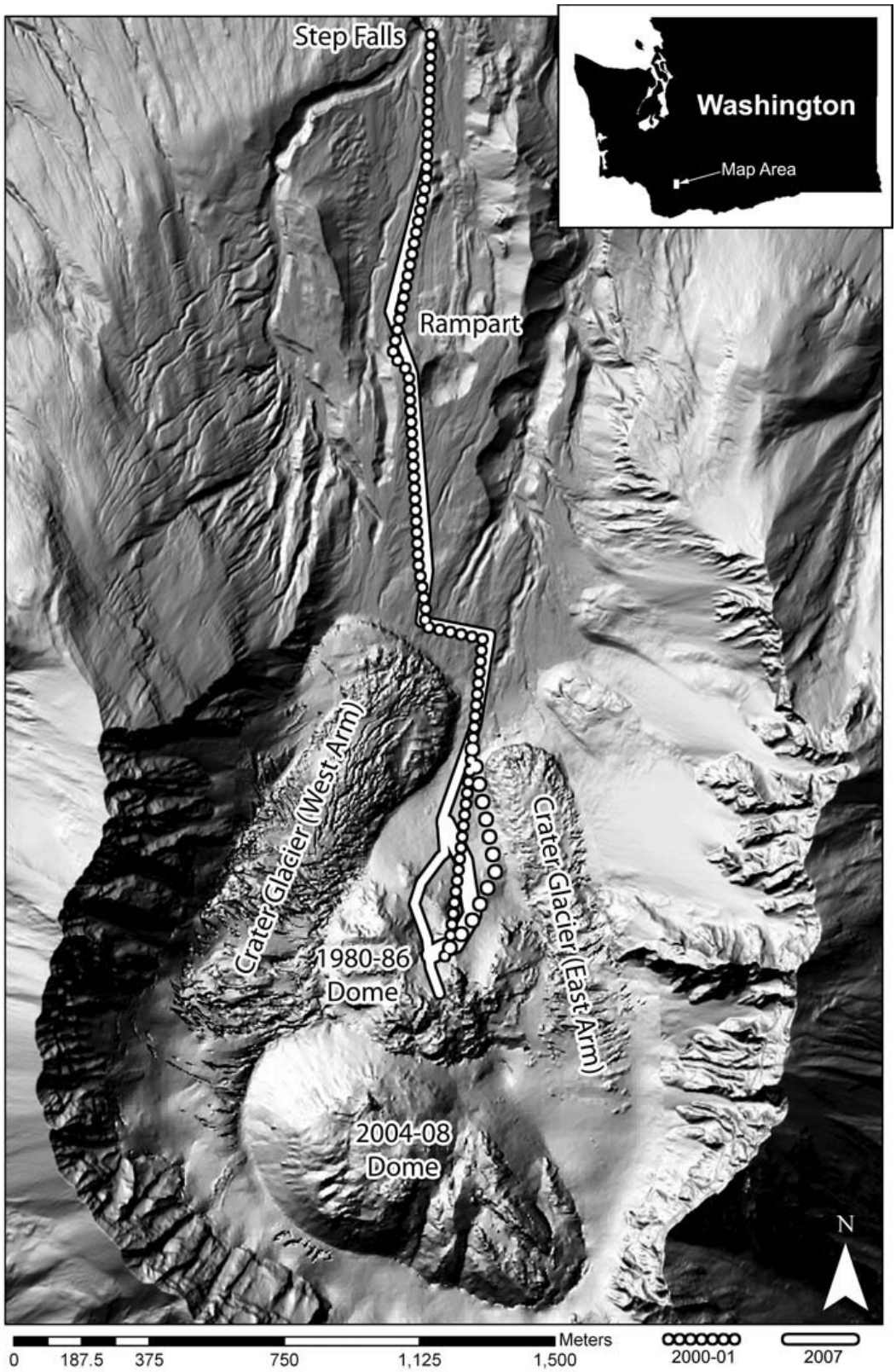

Figure 5.2. Location map of self-potential measurements reduced to two main lines, and two more secondary lines at the dome. Line type is the same as in Figure 5.3.

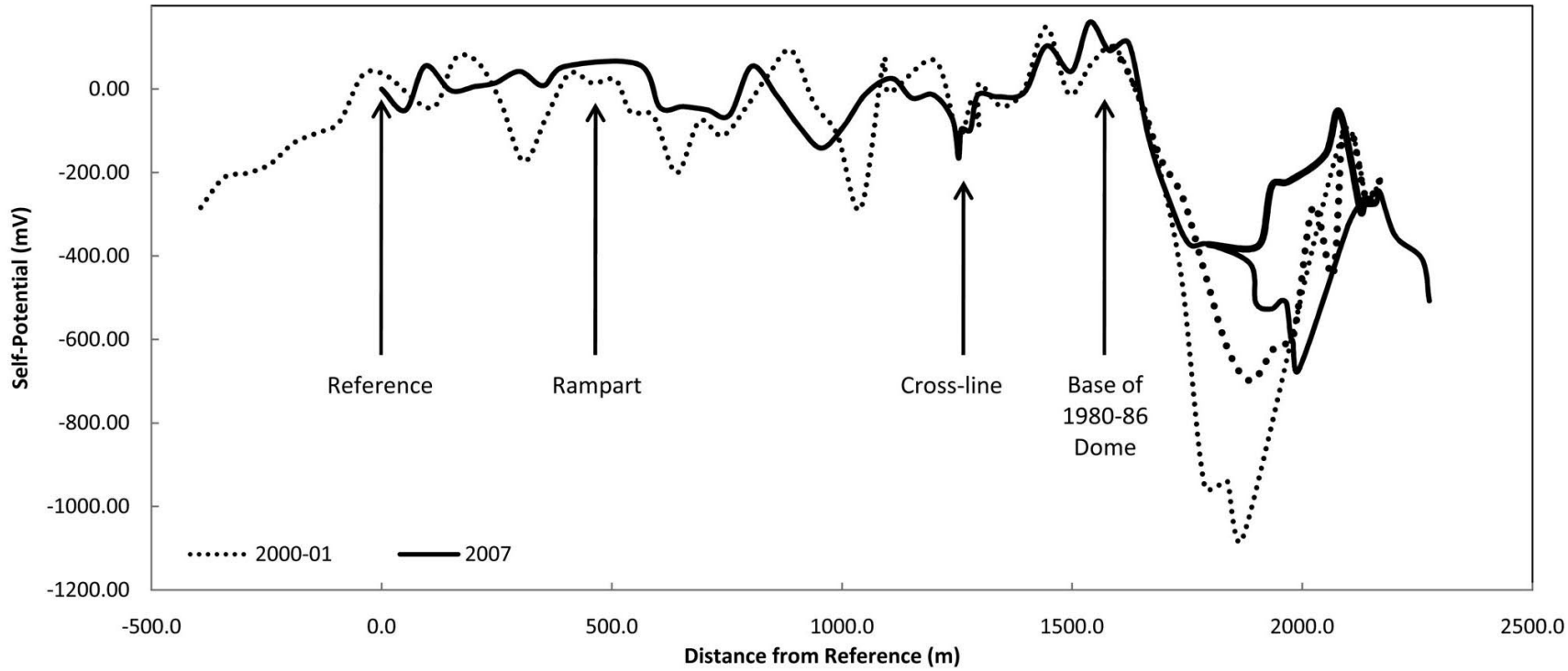

Figure 5.3. Both datasets reduced to two main lines on the crater floor and four lines on the dome as in Figure 5.2, with major features noted.

The two lines that resemble each other most between the two datasets (the thick dotted line from 2000-01 and the thin line from 2007) are located on opposite ends of the dome from each other. The other two lines that are furthest separated in self-potential signal happen to be the closest spatially. It seems that though the data on the crater floor are two-dimensional, the anomaly on the crater is perhaps more three-dimensional. Because no perpendicular data exist on the dome, and because the data vary quite a bit spatially over the dome, another way to visualize the anomaly on the dome is in two-dimensional map view.

Figure 5.4 shows both datasets in map view, with the surface kriged using Surfer. As noted above, the data agree well laterally and between sets on the crater floor. This, however, is not the case on the dome. The value of self-potential on the dome in 2000-2001 was considerably lower and more pronounced than in 2007. Although there were discrepancies on the dome, the two datasets were merged to create the map to provide maximum spatial coverage of the dome. On this map, the two minima on the dome are closer to -800 mV as opposed to the measured -1300 mV in 2000. It is possible that the map shown in Figure 5.4 is not indicative of the actual anomaly as it was in either 2000 or 2007, but spatial coverage on the dome for either survey separately was not enough to create a reliable map.

A final note of interest in the data is the radial extent of the negative anomaly in both 2000-01 and 2007. While the maximum amplitude of the anomaly (between -700 and 1300 mV) agrees well with anomalies on other volcanoes, the width of this anomaly is extremely narrow. Self-potential anomalies on Iwate, Iwaki, Nante, and Nikko-shirane volcanoes are of the same amplitude (-800 to -1900 mV) but have 1 to 2 km full width at

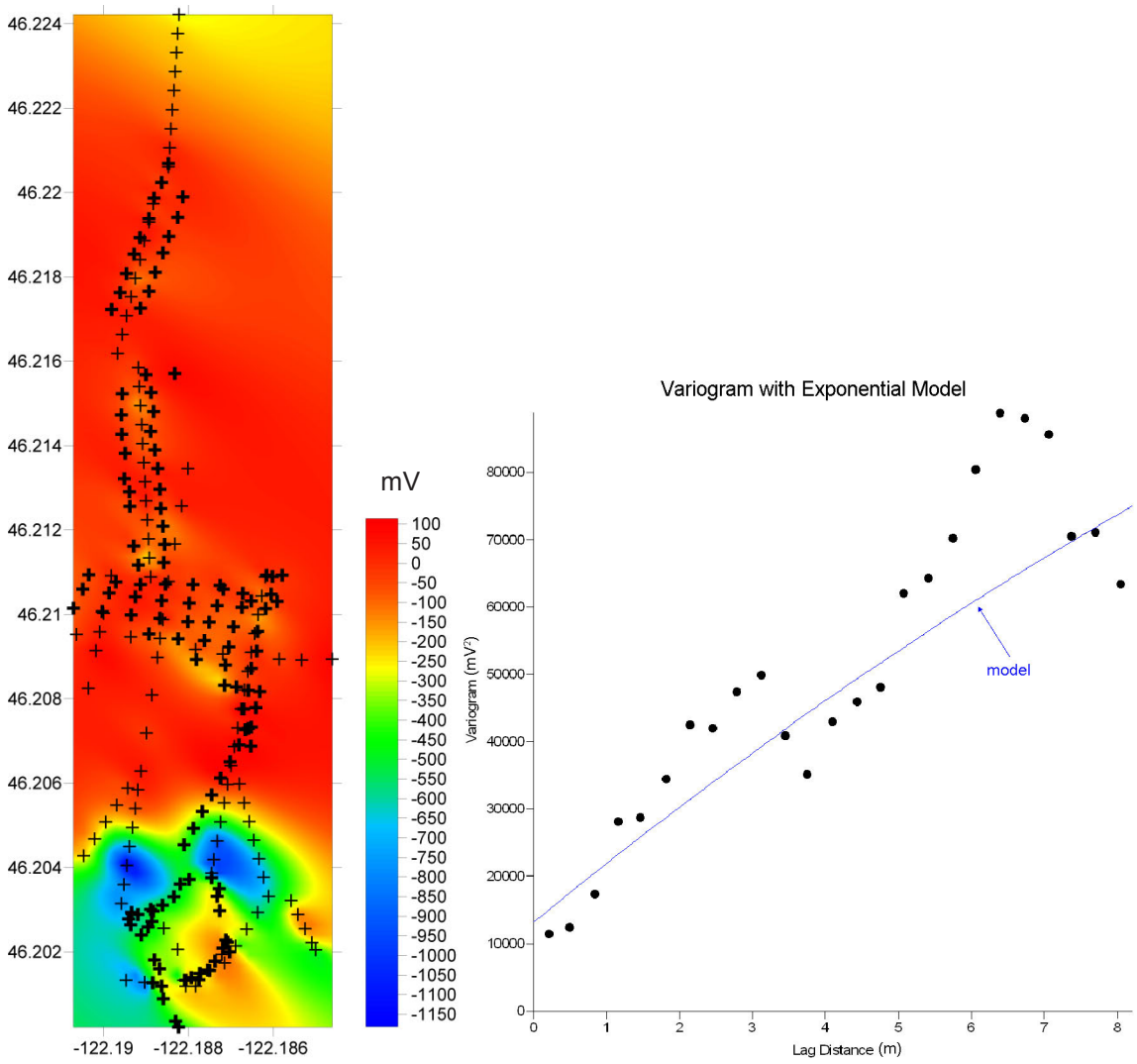

Figure 5.4. Data shown in map view, kriged using Surfer. Locations are marked with a cross, with bold crosses indicating the 2007 dataset. The variogram and model used for kriging are included at right.

half maximum (or minimum in this case) of the anomaly (Aizawa et al., 2009). On Mount St. Helens, the full width at half maximum of the anomaly is approximately 500 m, less than half of the width on other similar volcanoes.

A possible explanation is that the downward flow on Mount St. Helens is more vertically oriented than on other volcanoes, aided by a large, vertical fault zone. Figure 5.5 shows the location of a possible fault with respect to the location of the anomaly. This

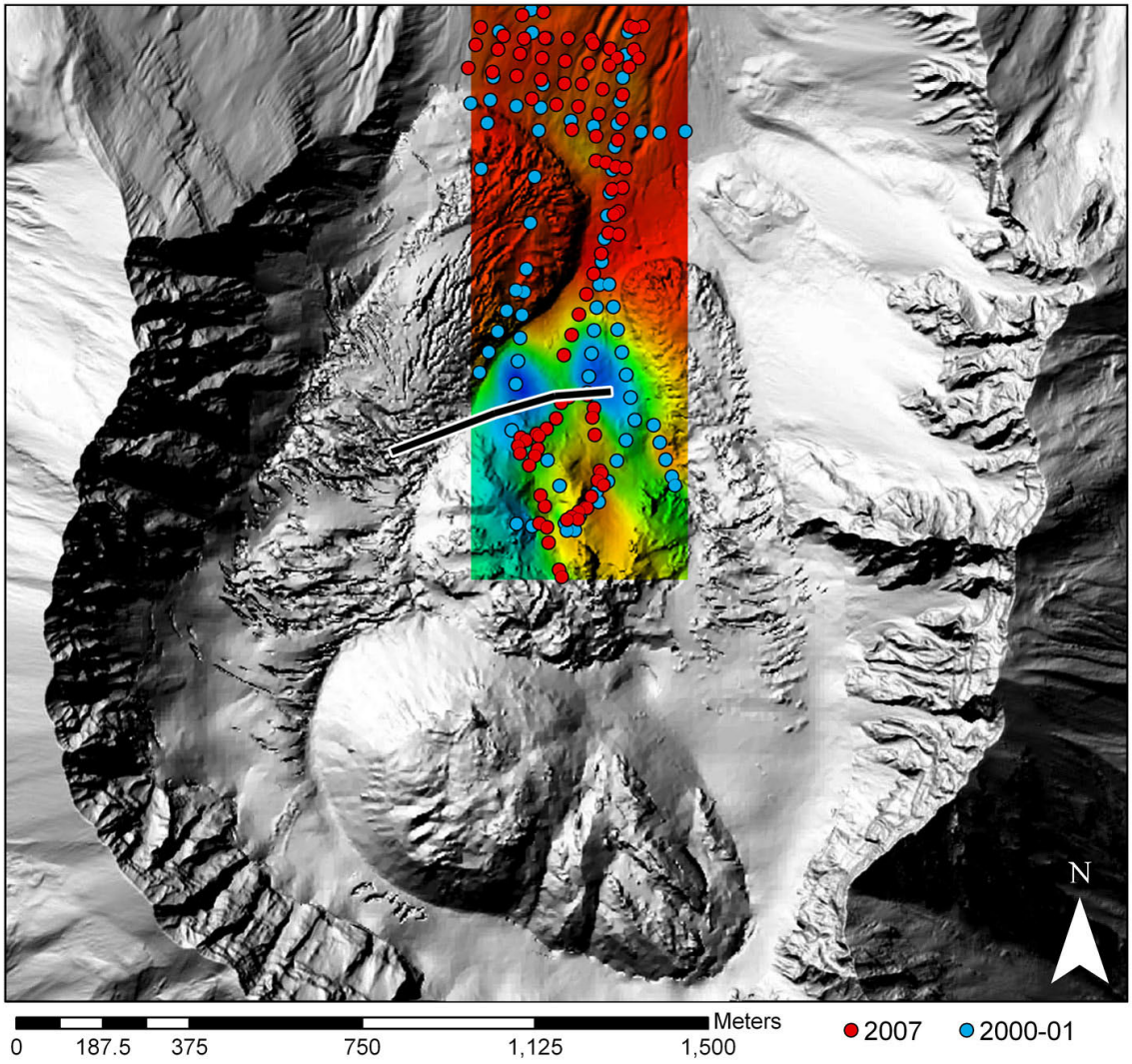

Figure 5.5. Map of crater and locations of measurements overlaid by combined self-potential map. Heavy line indicates approximate location of a fault scarp buried by the 1980-86 dome and glacier.

fault, called the Rampart Scarp (not to be confused with the rampart located nearly 1 km north in the breach), is a large thrust fault that was buried by the 1980-86 dome (Chadwick and Swanson, 1989). A cross-section of this thrust fault is shown in Figure 5.6, with self-potential above to emphasize the spatial correlation.

A large field of smaller, radial cracks and thrust faults surround the base of the 1980-86 dome, but do not extend further north than this fault. The spatial correlation of the

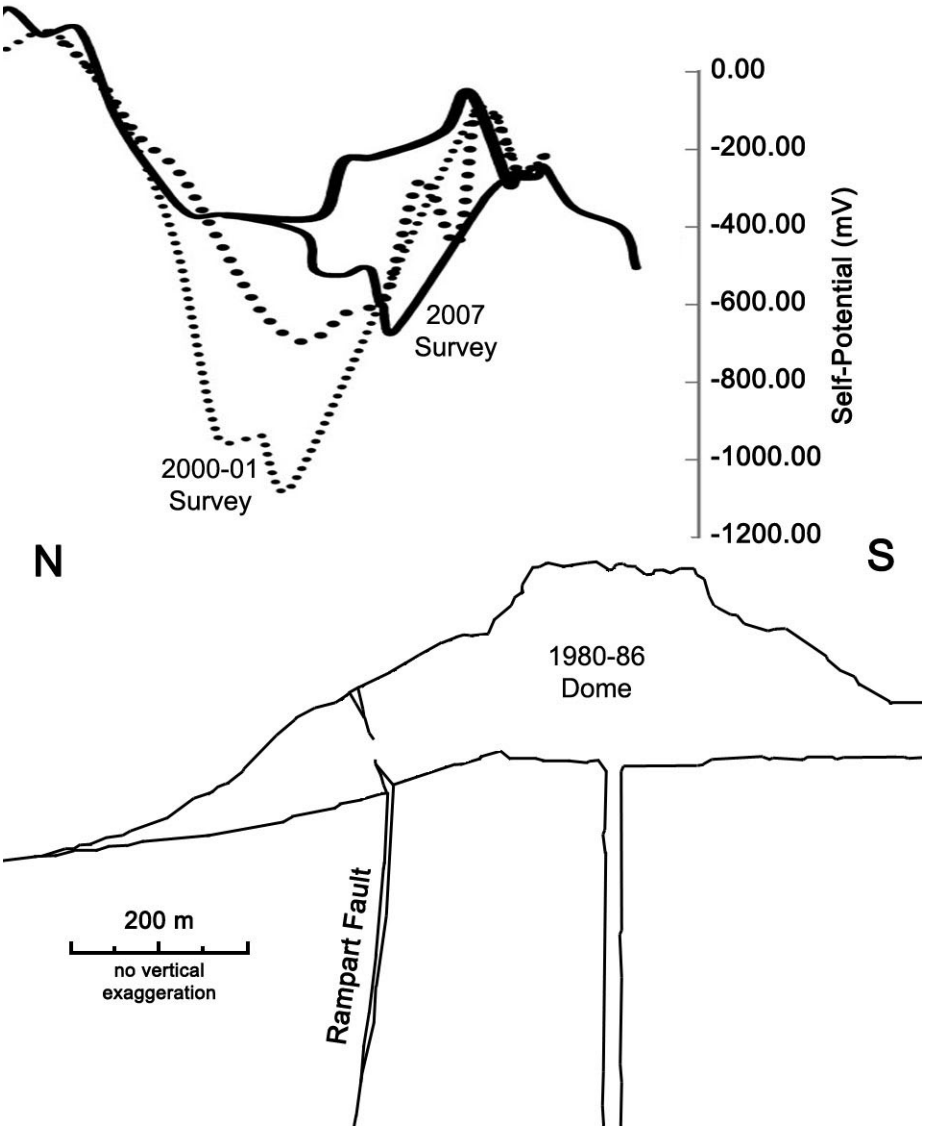

Figure 5.6. Cross-sectional view of the Rampart Fault, reproduced from Mastin (1994), with corresponding self-potential anomaly as in Figure 5.3.

location of this fault relative to the location of the 2007 self-potential low is extremely good. The role of the Rampart Fault as a conduit for the downward flow of water based on its location near the self-potential low is discussed in Section 5.4.

5.3 Electrical Resistivity from Time-Domain Electromagnetic Measurements

The TDEM data were processed and inverted for resistivity by Matt Burgess (San Diego State University). Measured data were converted to resistivity vs. time graphs and

each loop was independently inverted for one dimensional resistivity models using the SiTEM/Semdi inversion package from Aarhus Geophysics (Bedrosian et al., 2008).

Figure 5.6 shows the results of four layer inversion models of 25 loops in an approximately north-south line. Self-potential along the line is also shown. The resistivity structure appears to be very laterally homogeneous, which is not surprising given the lack of change in self-potential. In general, the one-dimensional structure consists of a surface resistive layer, two conductive layers, and a resistive layer beneath that. The surface resistor definitely consists of 1980 lahar and pyroclastic deposits, described in Hausback (2000) as unconsolidated or poorly consolidated flows of widely varying grain sizes, from a few mm to as large as 1 m in diameter. Both flows total as much as 30 m thick and were visible at the surface. These units are likely laid over debris flows, more pyroclastic flows, and the May 18, 1980 debris avalanche, which contain blocks as large as 100 m in diameter supported in a poorly sorted matrix. These five layers total as much as 140 m thick. This thickness agrees well with at least the thickness of the top resistive layer, and could possibly extend into the top conductor.

Bedrosian et al. (2008) attribute the top conductor to an aquifer either within the 1980 deposits, or just below them. The bottom conductor is assumed to be of Castle Creek age or older, and may possibly be an aquifer within a brecciated andesite or basalt (Bedrosian et al., 2008). However, the low resistivity of the layer (< 1 Ωm) indicates the probable presence of clay due to hydrothermal alteration, and may be a barrier to subsurface flow rather than a conduit. The bottom resistive layer is assumed to be of Pine Creek age or older (Bedrosian et al., 2008).

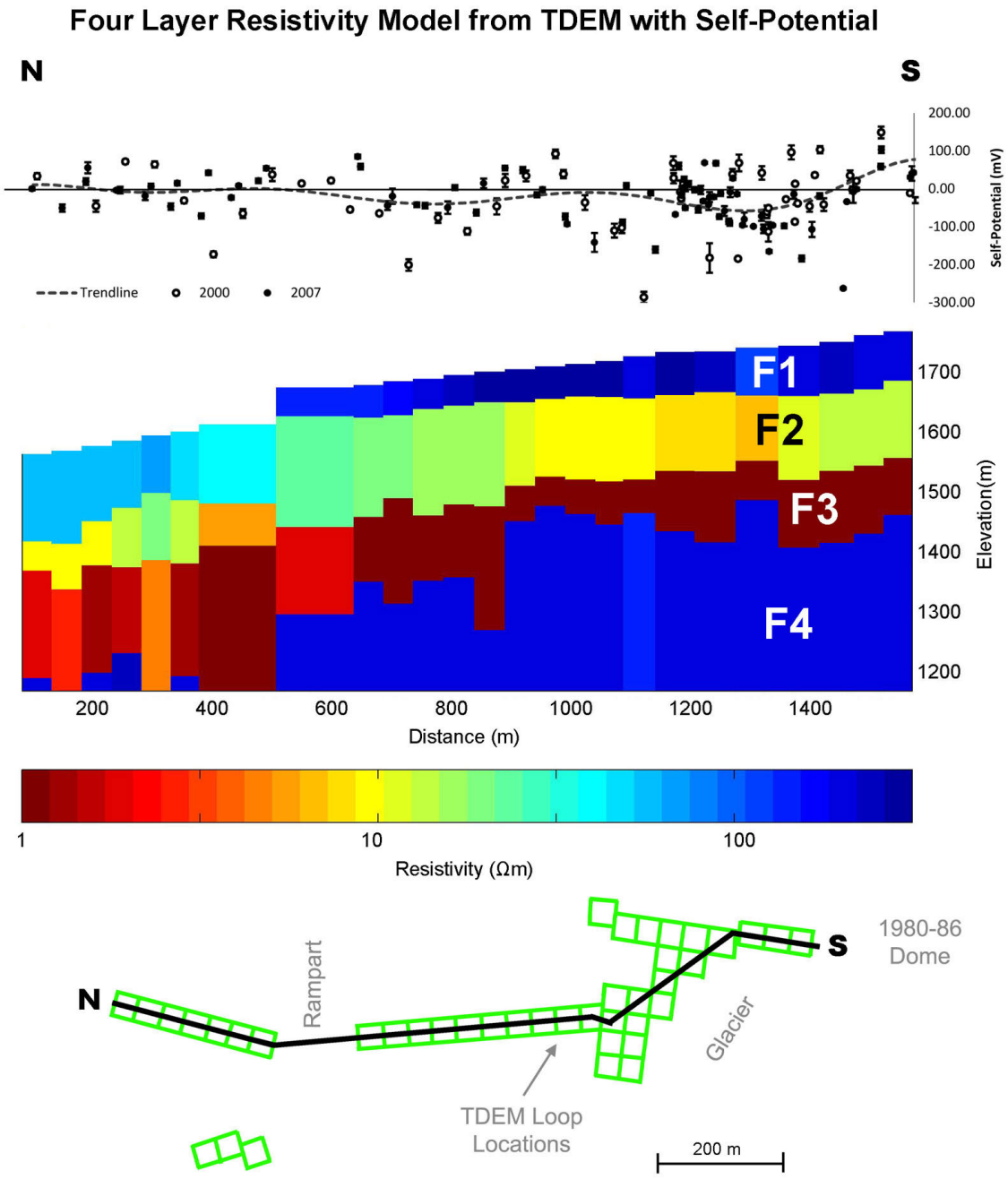

Figure 5.7. Four-layer resistivity structure from the 1-D inversion of TDEM data (center), self-potential (top), and relative location of cross-section (bottom). Modified from (Bedrosian et al., 2008).

5.4 Initial Results

Comparison of the two self-potential datasets reveals little change in the structure of the hydrothermal system, even in the presence a dome-building event only a few hundred meters south of the main anomaly. The change in the width and amplitude of the dome anomaly could probably be attributed to a change in heat flux or structure to the south of the data, but it seems that the structure north of the 1980-86 dome has remained unchanged, and continues to produce a large self-potential anomaly.

Given an interpretation of the TDEM and the behavior of the self-potential, we can begin to build a rough, simplified model of the groundwater flow in Mount St. Helens. Figure 5.7 is an example of one such model. The model is constrained by the four layer resistivity model from TDEM in the northern half, with the addition of a welded pyroclastic flow acting as a possible bottom seal to the aquifer. Lack of TDEM in the vicinity of the dome restricts how far we can safely assume the layers extend near and beneath the dome. Self-potential indicates upward flow of exsolved water from the conduit feeding the domes, and downward flow through the aquifer on the flanks, but primarily down the Rampart Fault. Mastin (1994) proposed that the Rampart Fault was, in part, responsible for shallow ($1.44 – 2.10 \pm 0.3$ km source depth) explosions on the dome caused by rapid water infiltration following storms. It follows that it is a likely conduit to downward water flow in the hydrothermal system now that heat from the eruption has subsided.

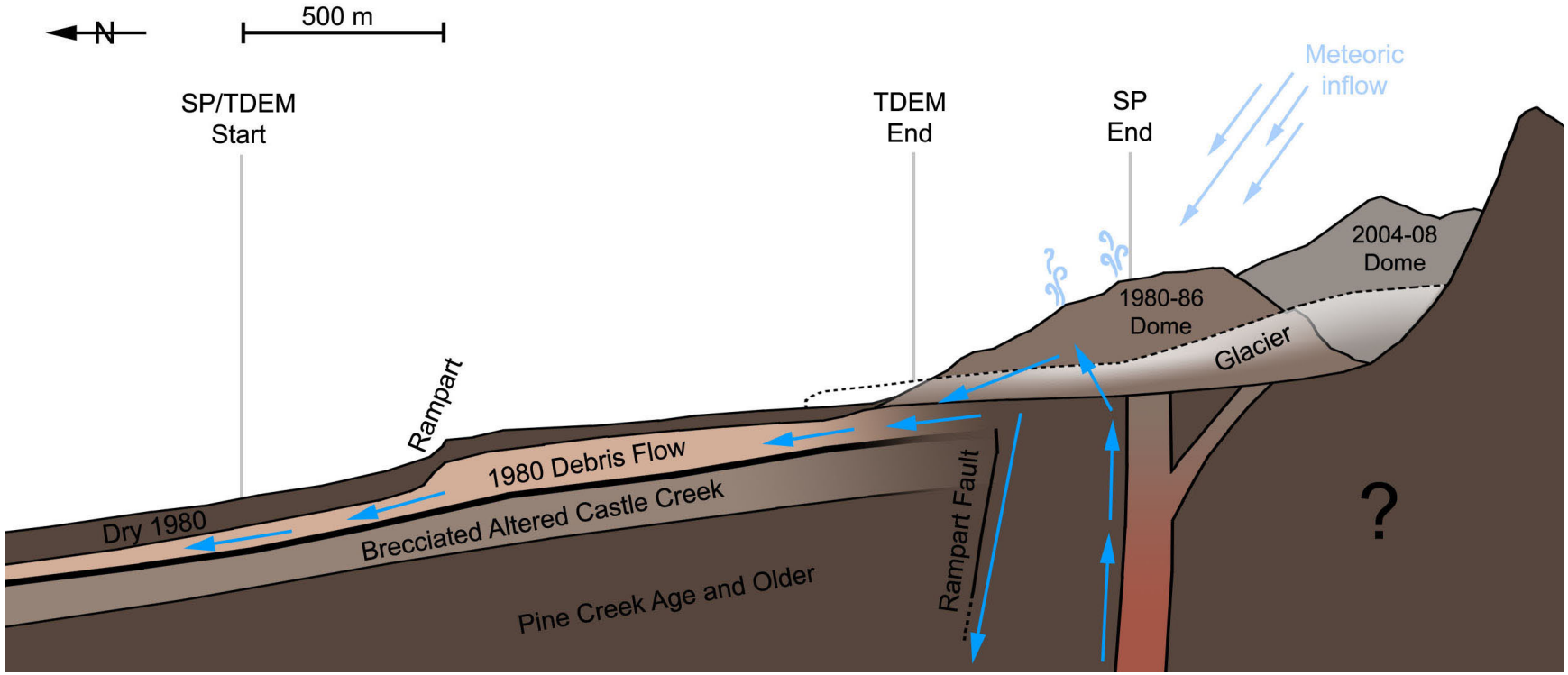

Figure 5.8. Cross-section of possible hydrogeologic system in Mount St. Helens, approximately 1:1 scale. Locations of data constraints are marked.

CHAPTER 6
NUMERICAL MODELING

Because the resistivity structure near the large self-potential anomaly on the dome is unknown, inverting for the causative groundwater flow would be very difficult for the area in which we are most interested. Instead, a better approach might be to check the validity of the proposed model in Figure 5.8 with a forward model and compare the results with the data. Forward modeling was conducted using COMSOL Multiphysics®.

6.1 COMSOL Multiphysics Finite Element Code

COMSOL Multiphysics® is a commercial finite element code that can solve a variety of coupled partial differential equations given geometry, physical properties of each subdomain, initial conditions, and boundary conditions. Geometry is defined using drawing tools, and both two- and three-dimensional geometries can be defined. Subdomains are subsets of the geometry that have different physical properties such as layers of stratigraphy. Multiple differential equations can be solved for simultaneously using the same geometry, and coupled processes can be linked with relative ease. In this case, groundwater flow using Darcy's Law (Earth Science Module, Darcy Flow) was linked to Ohm's Law (DC) to create a model of self-potential by solving the Poisson equation for the self-potential field (COMSOL, 2008).

6.2 Model Setup

The first step in setting up the forward model is defining the geometry. Although it seems that the main self-potential anomaly has some radial symmetry, a purely two-dimensional model was created similar to the model proposed in Figure 5.8. The TDEM

resistivity cross-sections were used to give approximate thicknesses of the strata near the north end of the model. Figure 6.1 shows the model geometry used in the forward model, with subdomains labeled in similar fashion as in Figure 5.7.

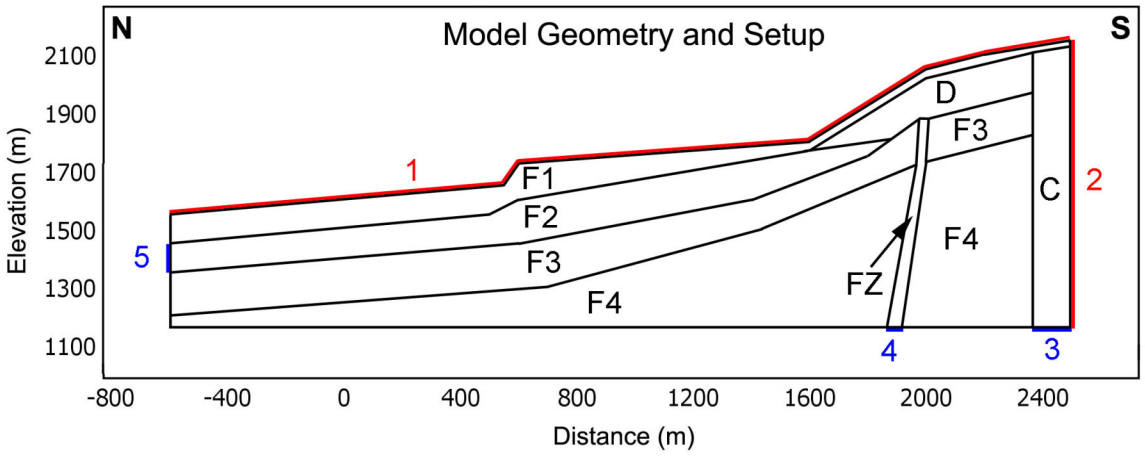

Figure 6.1. Model geometry used for COMSOL simulation. Subdomains are labeled as in Figure 5.8 and described in Table 6.1. Boundary conditions are described in-text.

Once the geometry of the model was set up, the next step was defining values for the physical properties of each subdomain, especially permeability and resistivity. Table 6.1 describes the properties used in the final forward model.

Table 6.1. Layer parameters used for COMSOL modeling.

Layer	Description	Resistivity (Ω-m)	Permeability (m^2)
F1	Dry 1980 deposits	100	1e-13
F2	Aquifer within 1980 deposits	10	1e-10
F3	Altered, brecciated Castle Creek	0.1	1e-18
F4	Pine Creek and older deposits	100	1e-13
FZ	Fault zone	10	1e-9
C	Conduit	10	1e-9
D	Dome	10	1e-10

Resistivity from the TDEM sections were used on the north end of the model, and were carried over into the southern end of the model. The dacite dome, conduit, and fault zone were given the same resistivity as the aquifer to reflect their similar composition and

water content. One modification from the TDEM resistivity was the value of resistivity in the possible clay layer, which was decreased slightly to reflect its clay content, especially near the dome. Permeability was significantly more difficult to assign, so values were approximated based on values used in modeling in Aizawa et al. (2009). Additionally, I assumed for simplicity that subdomains with flowing water were more permeable than those without, and that the clay layer was essentially impermeable to flow. The simulated self-potential was not particularly sensitive to the permeability, so trying to fine tune an appropriate permeability structure was not the focus of the modeling.

Next, boundary conditions for the model needed to be set. Figure 6.1 also shows the boundary conditions used for both the electric field and groundwater flow. Boundary 1, the earth's surface, was defined such that electrical current could not flow across it. Boundary 2 at the southernmost edge of the model was set to -100 mV to reduce edge effects, and all other boundaries were set to electrical ground under the assumption that the boundaries are far enough away from the main anomalies of interest. Boundary 3 is set as the source of groundwater flow, with inward flux equal to 5e-4 m/s over a width of 100 m. Boundaries 4 and 5 are sinks of groundwater flow, forcing water to flow up the conduit and then down the fault zone and the aquifer. Boundary 4 is set to a larger value (1e-3 m/s) than Boundary 5 (9e-5 m/s), both because it is a smaller boundary (50 m wide instead of 100 m), and because the self-potential data suggest that the downward flow is very strong. Flow rates were chosen experimentally, as the simulated self-potential was extremely sensitive to these rates. Trial and error was used to find flow rates that produced a stable signal and where the water was approximately conserved within the system. Water input from meteoric sources or introduced by glacial melt were not

included. The groundwater flow produced by these boundary conditions is shown in Figure 6.2.

Once subdomain and boundary conditions for electric field and groundwater flow were met individually, the two fields needed to be linked. This was achieved by setting the source current, $\vec{j}_s$, to be equal to $\overline{Q}_v\vec{u}$, as in Equation 3.1, where $\vec{u}$ is the calculated Darcy velocity from the groundwater flow model, and $\overline{Q}_v$ is the excess charge per unit

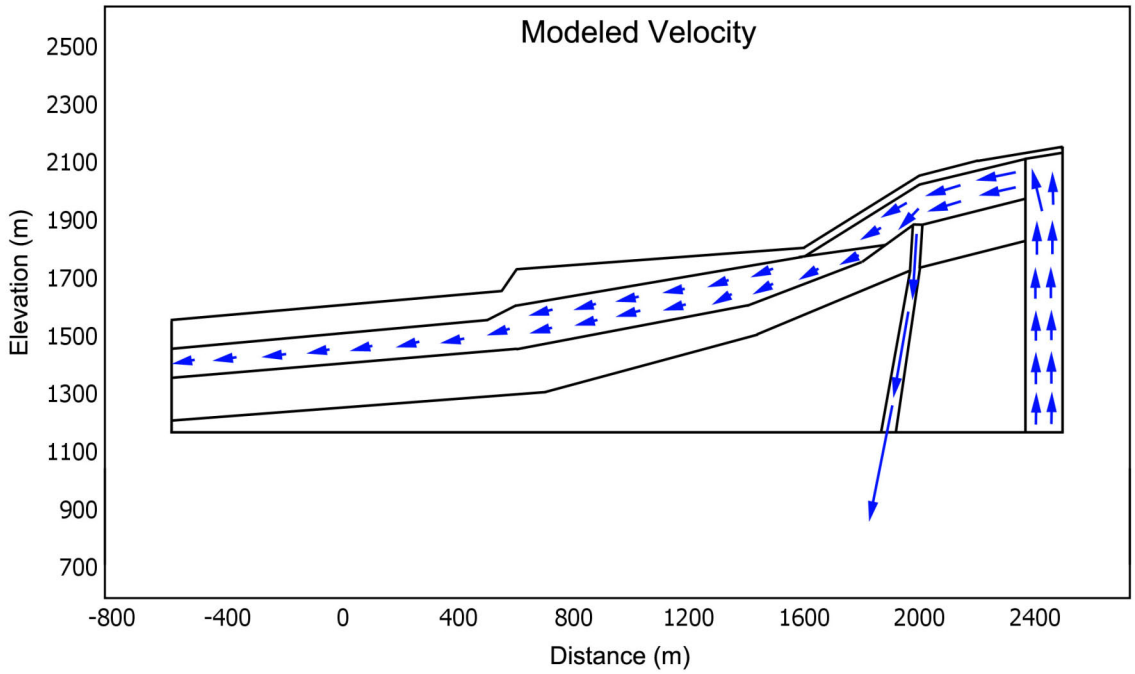

Figure 6.2. Forced groundwater flow used to model the self-potential response. Maximum flow is approximately 1e-3 m/s.

volume (C/m^3). $\overline{Q}_v$ was calculated according to the following equation modified from Jardani et al. (2007):

$$\overline{Q}_v = C\eta/\rho k \tag{6.1}$$

where C is the streaming potential coupling coefficient (mV/MPa), η is the dynamic viscosity of the fluid (Pa-s), ρ is resistivity (Ω-m), and k is permeability. The value of η was given the default value of 0.001 Pa-s by COMSOL, and the resistivity and

permeability for each subdomain were used to calculate $\overline{Q}_v$. C, the coupling coefficient, is thought to be approximately equal to -290 mV/MPa on Mount St. Helens (Bedrosian et al., 2007).

During modeling, it was found that the values for the self-potential anomaly were too low compared to the data. Instead of increasing the values of the groundwater flow at the boundaries, a factor of 3.5 was multiplied into $\overline{Q}_v$ to increase the potential caused by the existing groundwater flow. This factor can most likely be attributed to the assumed round values of permeability or resistivity being too high, within less than one order of magnitude each.

6.3 Model Results

After several different iterations of model shape and values, a final forward model was created that produced modeled self-potential values very close to the acquired data. A strongly negative self-potential anomaly was created on the surface in the vicinity of the fault. It was noted during modeling that the size and shape of the self-potential anomaly was very sensitive to the resistivity of the clay layer (F3). When the resistivity of this layer was decreased, the anomaly both increased in amplitude, and decreased in width.

Figure 6.3 shows the self-potential observed at the surface boundary overlaid on the actual acquired data. The model values were increased by several mV to adjust for the location of the reference potential. The model fits the overall trend of the data extremely well. Differences between the data and the model can easily be attributed to lateral heterogeneities in resistivity, permeability, and groundwater flow that are not reflected in

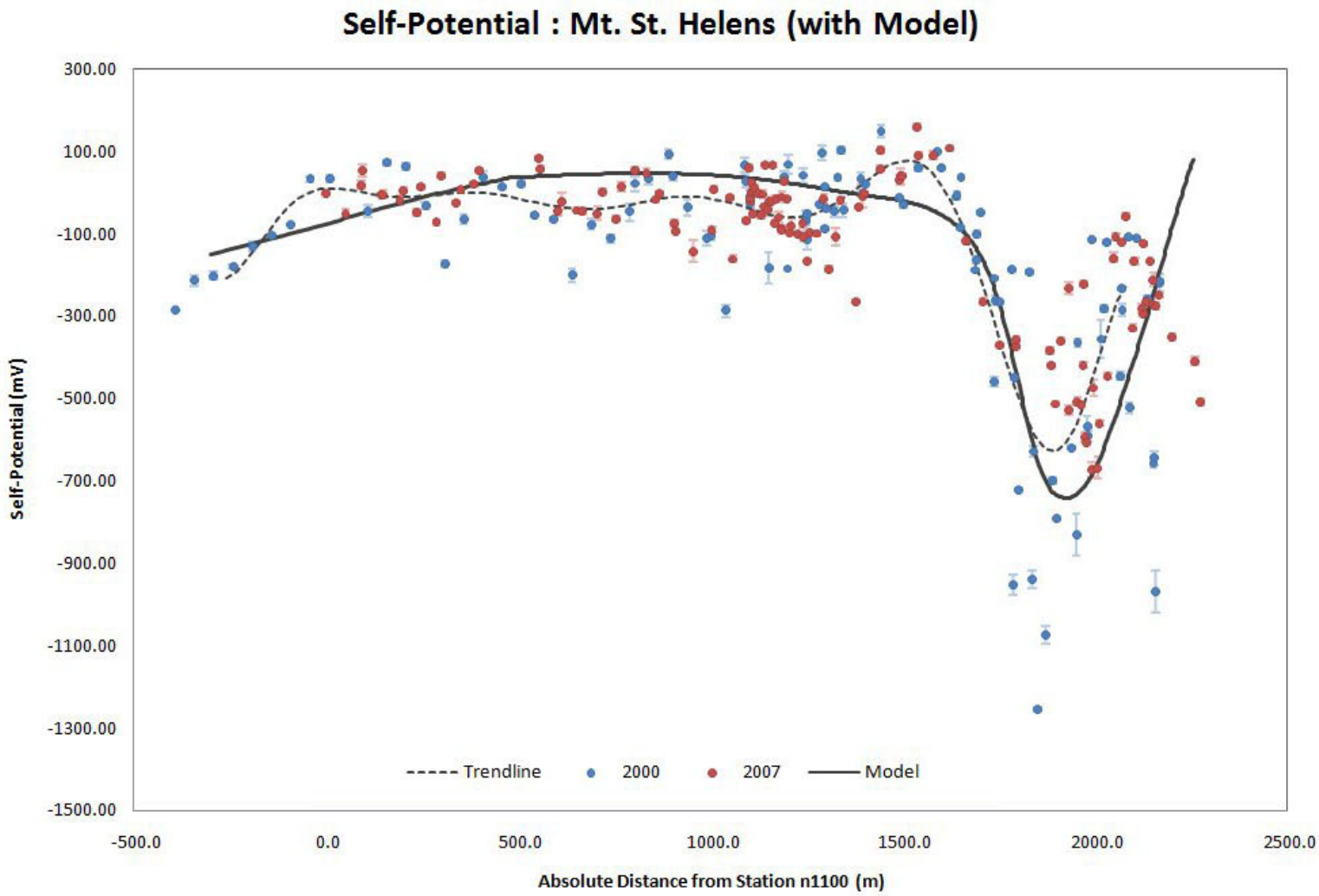

Figure 6.3. Resulting self-potential observed at the surface of the forward model overlaid on the acquired self-potential data. Fit of the data is to the first order, with finer structures in the self-potential signature not resolved.

the model. Another difference between the data and the model is noticeable between 1200 and 1600 m. The data seem to trend slightly downward to a local minimum near 1250 m, and then increase above the model to a local maximum at 1600 m before dipping into the main anomaly. The cause of this secondary dipolar feature is unknown, and is not reflected in the model.

6.4 Modeling Discussion

Though the model presented fits the data well, it is only one of any number of possible models that could fit the data equally well. This is mostly due to the lack of constraints on the parameters, especially permeability and resistivity near the dome, as well as the inherent nonuniqueness of the self-potential inverse problem. Also, values for the flux of water at the boundaries are unknown, and were mostly determined by trial and error based on the values of the produced self-potential signal. The values of these velocities appear to be very high but if groundwater velocity were decreased in the model, other values such as permeability and resistivity would need to be increased to account for the change. Additionally, the effects of heat, two-phase flow, and layers within the dome were not incorporated into the design of the model. Future modeling could be done to incorporate these effects, as well as check the plausibility of other different models.

The shape and size of the anomaly between the data and the model show promise that the Rampart Fault is the probable cause of downward flow in the system. The hydrothermal circulation inferred from the modeling of self-potential on volcanic edifices done by Ishido (2004) and Aizawa et al. (2009) do not seem to fit the peculiarly shaped anomaly on Mount St. Helens. The model proposed here indicates that the existence of a

deep, broad hydrothermal system does not seem to be the case on Mount St. Helens. Instead, a small, contained, yet powerful system exists very close to the conduit, with downward flow accommodated by a large fault system.

CHAPTER 7
CONCLUSIONS

The self-potential data acquired and the numerical modeling done to fit the data offer some interesting conclusions about the structure of the hydrothermal system in Mount St. Helens. This chapter outlines the main conclusions and offers recommendations for future research on the topic.

7.1 Discussion

Self-potential data from both the 2000-2001 and the 2007 surveys indicate the existence of a hydrothermal cell located near the 1980-86 dome. Although the self-potential anomaly in 2007 was of slightly less magnitude than in 2000-2001, the persistence of the anomaly indicates a remarkable resilience of the hydrothermal cell to a dome-building event only a few hundred meters to the south.

The size and shape of the self-potential anomaly compared to other volcanoes indicates that the hydrothermal system is shallow and well located, with the possibility that downward flow of water is controlled by a narrow fault zone close to the base of the 1980-86 dome. Structural observations of the crater floor before the formation of the 1980-86 dome revealed a large fault scarp that coincides well with the location of the self-potential anomaly. The Rampart Fault proves a good candidate for downward flow in the hydrothermal system.

Time-domain electromagnetic measurements showed the existence of a shallow aquifer in the crater floor overlaying a conductor. Information about the resistivity structure of the crater floor was then extrapolated to the dome to create a simplified model of groundwater flow in the crater and on the dome. This model was then used as

the basis of a forward model to recreate the self-potential signal caused by the groundwater flow. Results of the modeling indicate that the self-potential anomaly at the dome could have been caused by the downward flow of water in the Rampart Fault.

7.2 Future Work

While the forward modeling shows promising results, additional work can be done in this area to improve the model and attain more data to constrain it. The most significant shortcoming in the model is the lack of resistivity data on the dome. Though the slope of the dome was too steep to safely acquire TDEM data on foot, and the advance of the crater glacier has cut off access to the dome from the crater floor, it is conceivable that an airborne time-domain electromagnetic system, such as SkyTEM could be flown over the crater (Sørense and Auken, 2004).

Another shortcoming in the model is the lack of permeability data. Thankfully, outcrops of several of the assumed layers exist on the edifice, and samples could be attained. Additionally, laboratory measurements of $\overline{Q}_v$ for some of these samples could also be made to improve the quality of the model.

The forward model itself could also be improved to include the effects of heat flow and steam, since the current model does not account for either of these effects. Also, the model does not account for influx of rainfall or glacial melt into the system, or the outflow of hot springs and other surface features. Forward modeling could also be performed to test other models, such as the flow of water through a layered dome structure, or downward flow not controlled by the Rampart Fault. Additionally, we plan to perform a dipolar tomography on the self-potential data to further improve our model of groundwater flow.

Finally, more self-potential measurements could be taken on Mount St. Helens where no data currently exist. For example, more coverage on the 1980-86 dome could be completed over the course of a day with the aid of a helicopter. Coverage over the 2004-07 dome could be interesting as well, but is probably too dangerous at this point. Data could also be taken along the hiking trail on the southern slope of the volcano up to the top of the crater wall. Self-potential measurements along the southern face could provide more information about groundwater flow in that region of the volcano, which is conceivably more topographically driven. Continued measurements down the north face as well as the south would expand measurements to a full edifice scale. The only difficulty here would be finding a way to tie the two datasets together.

REFERENCES CITED

Aizawa, K., 2004. A large self-potential anomaly and its changes on the quiet Mt. Fuji, Japan. Geophysical Research Letters, 31: L05612, doi:10.1029/2004GL019462.

Aizawa, K., Ogawa, Y. and Ishido, T., 2009. Groundwater flow and hydrothermal systems within volcanic edifices: Delineation by electric self-potential and magnetotellurics. Journal of Geophysical Research, 114: B01208, doi:10.1029/2008JB005910.

Aizawa, K. et al., 2005. Hydrothermal system beneath Mt. Fuji volcano inferred from magnetotellurics and electric self-potential. Earth and Planetary Science Letters, 235(1-2): 343-355.

Anderson, L.A., Johnson, D.J. and Dzurisin, D., 1983. Self-potential and VLF electromagnetic surveys at Mount St. Helens, Washington [abstract]. Eos, Transactions, American Geophysical Union, 64(45): 894-895.

Barde-Cabusson, S., A. Finizola, A. Revil, T. Ricci, S. Piscitelli, E. Rizzo, B. Angeletti, M. Balasco, L. Bennati, S. Byrdina, N. Carzaniga, A. Crespy, F. Di Gangi, J. Morin, A. Perrone, M. Rossi, E. Roulleau, B. Suski, and N. Villeneuve, 2009. New geological insights and structural control on fluid circulation in La Fossa cone (Vulcano, Aeolian Islands, Italy). Journal of Volcanology and Geothermal Research, 185: 231-245.

Bedrosian, P.A., Burgess, M. and Hotovec, A., 2008. Groundwater Hydrology within the Crater of Mount St. Helens. Eos, Transactions, American Geophysical Union, 89(53): Fall Meet. Suppl., Abstract V43E-2191.

Bedrosian, P.A., Unsworth, M.J. and Johnston, M.J.S., 2007. Hydrothermal circulation at Mount St. Helens determined by self-potential measurements. Journal of Volcanology and Geothermal Research, 160(1-2): 137-146.

Brantley, S.R. and Myers, B., 2000. From the 1980 Eruption to 2000: U.S. Geological Survey Fact Sheet-036-00, 2 p.

Byrdina, S., S. Friedel, J. Wassermann, and J. Zlotnicki, 2003. Self-potential variations associated with ultra-long-period seismic signals at Merapi volcano. Geophysical Research Letters, 30(22): 2156, doi:10.1029/2003GL018272.

Castermant, J., C.A. Mendonça, A. Revil, F. Trolard, G. Bourrié, and N. Linde, 2008. Redox potential distribution inferred from self-potential measurements associated with the corrosion of a metallic body. Geophysical Prospecting, 56: 269-282.

Chadwick, W.W. and Swanson, D.A., 1989. Thrust faults and related structures in the crater floor of Mount St. Helens volcano, Washington. Geological Society of America Bulletin, 101: 1507-1519.

COMSOL, 2008. COMSOL Multiphysics User's Guide. Stockholm: COMSOL AB.

Clynne, M.A. et al., 2008. The Pleistocene Eruptive History of Mount St. Helens, Washington, from 300,000 to 12,800 Years Before Present. In: D.R. Sherrod, W.E. Scott and P.H. Stauffer (Editors), A Volcano Rekindled: The Renewed Eruption of Mount St. Helens, 2004-2006. U.S. Geological Survey Professional Paper 1750, pp. 25.

Clynne, M.A., Ramsey, D.W. and Wolfe, E.W., 2005. Pre-1980 Eruptive History of Mount St. Helens, Washington: U. S. Geological Survey Fact Sheet 2005-0345, 4 p.

Corwin, R.F. and Hoover, D.B., 1979. The self-potential method in geothermal exploration. Geophysics, 44(2): 226-245.

Davis, P.M., Dvorak, J.J., Johnston, M.J.S. and Dzurisin, D., 1989. Electric and magnetic field measurements on Mount St. Helens volcano at times of eruptions 1980-1985. Journal of Geomagnetism and Geoelectricity, 41(9): 783-796.

Di Maio, R., P. Mauriello, D. Patella, Z. Petrillo, S. Piscitelli, and A. Siniscalchi, 1998. Electric and electromagnetic outline of the Mount Somma-Vesuvius structural setting. Journal of Volcanology and Geothermal Research, 82: 219-238.

Ewert, J.W., Myers, B.M. and Brantley, S.R., 1994. Preparing for the next eruption in the Cascades: U.S. Geological Survey Open-File Report 94-585, 4 p.

Finizola, A., F. Sortino, J.-F. Lénat, and M. Valenza, 2002. Fluid circulation at Stromboli volcano (Aeolian Islands, Italy) from self-potential and CO_2 surveys. Journal of Volcanology and Geothermal Research, 116: 1-18.

Finizola, A., F. Sortino, J.-F. Lénat, M. Aubert, M. Ripepe, and M. Valenza, 2003. The summit hydrothermal system of Stromboli. New insights from self-potential, temperature, CO_2 and fumarolic fluid measurements, with structural and monitoring implications. Bulletin of Volcanology, 65: 486-504.

Finizola, A., J.-F. Lénat, O. Macedo, D. Ramos, J.-C. Thouret, F. Sortino, 2004. Fluid circulation and structural discontinuities inside Misti volcano (Peru) inferred from self-potential measurements. Journal of Volcanology and Geothermal Research, 135: 343-360.

Fox, R.W., 1830. On the electromagnetic properties of metalliferous veins in the mines of Cornwall. Philosophical Transactions of the Royal Society, 120: 399-414.

Gerstenecker, C., Tiede, C., Läufer, G., Wrobel, B. and Steineck, D., 2004. Proc. 1st Ass. EGU.

Hase, H., T. Hashimoto, S. Sakanaka, W. Kanda, and Y. Tanaka, 2005. Hydrothermal system beneath Aso volcano as inferred from self-potential mapping and resistivity structure. Journal of Volcanology and Geothermal Research, 143: 259-277.

Hashimoto, T. and Tanaka, Y., 1995. A large self-potential anomaly on Unzen volcano, Shimabara peninsula, Kyushu island, Japan. Geophysical Research Letters, 22(3): 191-194.

Hausback, B.P., 2000. Geologic Map of the Sasquatch Steps Area, North Flank of Mount St. Helens, Washington, Geologic Investigations Series Map I-2463. U. S. Geological Survey.

Ishido, T., 2004. Electrokinetic mechanism for the W-shaped self-potential profile on volcanoes. Geophysical Research Letters, 31: L15616, doi:10.1029/2004GL020409.

Jardani, A. et al., 2006. Least squares inversion of self-potential (SP) data and application to the shallow flow of ground water in sinkholes. Geophysical Research Letters, 33: L19306, doi:10.1029/2006GL027458.

Jardani, A. et al., 2007. Tomography of the Darcy velocity from self-potential measurements. Geophysical Research Letters, 34: L24403, doi:10.1029/2007GL031907.

Lipman, P.W., Mullineaux, D.R. (Eds.), 1981. The 1980 Eruptions of Mount St. Helens, Washington. USGS. Prof. Paper 1250, 844 p.

López, D.L., and S.N. Williams, 1993. Catastrophic Volcanic Collapse: Relation to Hydrothermal Processes. Science, 260: 1794-1796.

Major, J.J., Scott, W.E., Driedger, C. and Dzurisin, D., 2005. Mount St. Helens Erupts Again; Activity from September 2004 through March 2005: U. S. Geological Survey Fact Sheet 2005-3036, 4 pages.

Mastin, L.G., 1994. Explosive tephra emissions at Mount St. Helens, 1989-1991: The violent escape of magmatic gas following storms? Geological Society of America Bulletin, 106: 175-185.

Massenet, F. and V.N. Pham, 1985. Experimental and Theoretical Basis of Self-Potential Phenomena in Volcanic Areas with Reference to Results Obtained on Mount Etna (Sicily). Earth and Planetary Science Letters, 73: 415-429.

Messerich, J.A., S.P. Schilling, R.A. Thompson, 2008. Digital Elevation Models of the Pre-Eruption 2000 Crater and 2004–07 Dome-Building Eruption at Mount St. Helens, Washington, USA: U. S. Geological Survey Open File Report 2008-1169, 2 pages.

Michel, S. and J. Zlotnicki, 1998. Self-potential and magnetic surveying of La Fournaise volcano (Réunion Island): Correlations with faulting, fluid circulation, and eruption. Journal of Geophysical Research, 103(B8): 17,845-17,857.

Minsley, B.J., Sogade, J. and Morgan, F.D., 2007. Three-dimensional source inversion of self-potential data. Journal of Geophysical Research, 112: B02202, doi:10.1029/2006JB004262.

Nyquist, J.E. and C.E. Corry, 2002. Self-potential: The ugly duckling of environmental geophysics. The Leading Edge, May 2002: 446-451.

Petiau, G., 2000. Second Generation of Lead-lead Chloride Electrodes for Geophysical Applications. Pure and Applied Geophysics, 157(3): 357-382.

Poldini, E., 1938. Geophysical exploration by spontaneous polarization methods. Min. Mag., 59: 278-282, 347-352.

Revil, A. and Jardani, A., 2009. The Self-Potential Method: Did the Ugly Duck of Environmental Geophysics Turn Into a Beautiful Swan?, EEGS Annual Meeting, Fort Worth, TX.

Revil, A. and Linde, N., 2006. Chemico-electromechanical coupling in microporous media. Journal of Colloid and Interface Science, 302(2): 682-694.

Revil, A., Schwaeger, H., Cathles, L.M., III and Manhardt, P.D., 1999. Streaming potential in porous media 2. Theory and application to geothermal systems. Journal of Geophysical Research, 104: 20033-20048.

Rizzo, E., B. Suski., A. Revil, S. Straface, and S. Troisi, 2004. Self-potential signals associated with pumping tests experiments. Journal of Geophysical Research, 109: B10203, doi:10.1029/2004JB003049.

Saba, M., Y. Nishida, T. Mogi, S. Takakura, and N. Matsushima, 2007. Development of geothermal field following the 2000 eruption of Usu volcano as revealed by ground temperature, resistivity and self-potential variations. Annals of Geophysics, 50(1): 79-92.

Sasai, Y., M. Uyeshima, J. Zlotnicki, H. Utada, T. Kagiyama, T. Hashimoto, and Y. Takahashi, 2002. Magnetic and electric field observations during the 2000 activity

of Miyake-jima volcano, Central Japan. Earth and Planetary Science Letters, 203: 769-777.

Schilling, S.P., Carrara, P.E., Thompson, R.A. and Iwatsubo, E.Y., 2004. Posteruption glacier development within the crater of Mount St. Helens, Washington, USA. Quaternary Research, 61(3): 325-329.

Siebert, L., H. Glicken, T. Ui, 1987. Volcanic hazards from Bezymianny- and Bandai-type eruptions. Bull. Volcanol. 49: 435-459.

Sill, W.R., 1983. Self-potential modeling from primary flows. Geophysics, 48(1): 76-86.

Sørense K.I., and Auken E., 2004. SkyTEM: a new high-resolution helicopter transient electromagnetic system. Exploration Geophysics, 35: 194–202.

Tilling, R.I., Topinka, L. and Swanson, D.A., 1990. REPORT: Eruptions of Mount St. Helens: Past, Present, and Future, U.S. Geological Survey Special Interest Publication, 56 p.

Topinka, L., 2008. Mount St. Helens Eruption 2004 - July 2008. URL: http://vulcan.wr.usgs.gov/Volcanoes/MSH/Eruption04/Monitoring/July2008/

White, J.D.L., 1996. Impure coolants and interaction dynamics of phreatomagmatic eruptions. Journal of Volcanology and Geothermal Research, 74: 155–170.

Zablocki, C.J., 1976. Mapping thermal anomalies by the self- potential method, Kilauea, Hawaii, in: The Development and Use of Geothermal Resources, Proc. U.N. Symp., Vol. 2, pp. 1299-1309.

Zlotnicki, J., Y. Sasai, P. Yvetot, Y. Nishida, M. Uyeshima, F. Fauquet, H. Utada, Y. Takahashi, and G. Donnadieu, 2003. Resistivity and self-potential changes associated with volcanic activity: The July 8, 2000 Miyake-jima eruption (Japan). Earth and Planetary Science Letters, 205(3-4): 139-154.

Zlotnicki, J., and Y. Nishida, 2003. Review on morphological insights of self-potential anomalies on volcanoes. Surveys in Geophysics, 24: 291-338.